nature neuroscience

Article

https://doi.org/10.1038/s41593-025-01937-y

Sequential and independent probabilistic events regulate differential axon targeting during development in *Drosophila melanogaster*

Received: 7 July 2023

Accepted: 3 March 2025

Published online: 7 May 2025

Check for updates

Maheva Andriatsilavo[1,2], Carolina Barata[3], Eric Reifenstein[3], Alexandre Dumoulin[4,5], Tian Tao Griffin[1], Suchetana Bias Dutta[1,2,7], Esther T. Stoeckli[4,5], Max von Kleist[3,6], P. Robin Hiesinger[2] & Bassem A. Hassan[1,2]

Variation in brain wiring contributes to non-heritable behavioral individuality. How and when these individualized wiring patterns emerge and stabilize during development remains unexplored. In this study, we investigated the axon targeting dynamics of *Drosophila* visual projecting neurons called DCNs/LC14s, using four-dimensional live-imaging, mathematical modeling and experimental validation. We found that alternative axon targeting choices are driven by a sequence of two independent genetically encoded stochastic processes. Early Notch lateral inhibition segregates DCNs into Notch^{ON} proximally targeting axons and Notch^{OFF} axons that adopt a bi-potential transitory state. Subsequently, probabilistic accumulation of stable microtubules in a fraction of Notch^{OFF} axons leads to distal target innervation, whereas the rest retract to adopt a Notch^{ON} target choice. The sequential wiring decisions result in the stochastic selection of different numbers of distally targeting axons in each individual. In summary, this work provides a conceptual and mechanistic framework for the emergence of individually variable, yet robust, circuit diagrams during development.

Although brain wiring patterns are similar between individuals, they are not identical. Analyses of neuronal morphology and connectivity within stereotypic wiring diagrams identified variations among neurons of the same types[1–4]. In all animals, including humans, such structural variation between brain hemispheres and among individuals sharing the same genetic and environmental background ensures behavioral individuality[5,6] while maintaining the population around an optimal mean for niche exploitation[6–8]. How and when these individualized wiring patterns emerge and stabilize during development remains largely unexplored. *Drosophila melanogaster* is a powerful model to investigate stochastic variation, individual behavior and the relationship. For example, flies exhibit individual sense of smell[9]. Although each olfactory interneuron class stereotypically innervates the *Drosophila* antenna lobe, individual neuron morphology varies across hemibrains[4,9]. Flies also display individual learning performance[10], and symmetry in the *Drosophila* central nervous system affects individual long-term memory[2].

[1]Institut du Cerveau-Paris Brain Institute (ICM), Sorbonne Université, Inserm, CNRS, Hôpital Pitié-Salpêtrière, Paris, France. [2]Division of Neurobiology of the Institute for Biology, Free University, Berlin, Germany. [3]Department of Mathematics and Computer Science, Free University, Berlin, Germany. [4]Department of Molecular Life Sciences, University of Zurich, Zurich, Switzerland. [5]Neuroscience Center Zurich, University of Zurich, Zurich, Switzerland. [6]Project Group 5 'Systems Medicine of Infectious Disease', Robert Koch Institute, Berlin, Germany. [7]Present address: Center for Regenerative Therapies Dresden, TU Dresden, Dresden, Germany. e-mail: bassem.hassan@icm-institute.org

Our previous work identified variations within the wiring patterns of a *Drosophila* visual projecting neuron type, called dorsal clustered neurons (DCNs)/LC14s[11,12], leading to individual visual response behaviors[3]. DCNs are commissural neurons divided in two morphologically and functionally distinct subtypes[11–13]: L-DCNs, whose axons terminate in the proximal optic lobe neuropile (lobula) (Fig. 1a,c,d), and M-DCNs, which further innervate distal targets (lobula plate (LP) and medulla) (Fig. 1b–d(i)). Each hemibrain contains a group of 22–68 DCN cell bodies[3,11]. Although both subtypes originate from a common progenitor[12,13], they vary non-proportionally between hemispheres and among individuals[3,11]. DCN subtypes are established post-mitotically[11] in part through a cell-based competition among immature neurons. However, when and how DCNs become irreversibly morphologically committed to L-DCN or M-DCN subfate during development remains unclear.

In this study, we explored the dynamic nature of DCN axon targeting using live imaging[14,15]. We found that two successive decisional steps, driven by independent stochastic processes, restrict DCN axon potential to innervate distal targets through time. We previously showed that Notch lateral inhibition in immature DCNs modulates adult DCN subtype outcome[11]. Here we show that early, but not late, activation of Notch signaling prevents medulla innervation. However, *Notch* loss of function does not deterministically convert an immature DCN into an M-DCN. Unlike classical binary fate choice models[16], Notch^{OFF} cells adopt an intermediate transitory state that can potentially innervate the medulla, indicating that at least one additional targeting choice contributes to stabilizing growing axons. Using data-driven mathematical modeling and experimental validation, we found that Notch^{OFF} axon terminals stabilize via a conserved probabilistic and competitive accumulation of stable microtubules. This results in the definitive consolidation of M-DCN morphology in a subset of neurons, whereas remaining Notch^{OFF} axons collapse to the lobula due to the absence of stable microtubules, thus adopting a Notch^{ON}-like subtype morphology.

Results

Targeting decisions occur before distal target innervation

L-DCN axons innervate the lobula, whereas M-DCNs further reach the medulla (Fig. 1a–d)[11–13]. To investigate how these two morphologically distinct subtypes emerge during development, we asked when and how this differential targeting choice is made. Two models[17] could explain DCN medulla innervation: a target-dependent mechanism, where axons first reach distal targets and retract if they fail to establish connections, or a target-independent mechanism, where distal targeting commitment occurs before reaching the medulla. To discriminate between these two hypotheses, we live imaged DCN axon development using intravital two-photon microscopy in intact animals[15] (Fig. 1f). We first determined the DCN target innervation timing, starting from the end of lobula innervation (30 h after pupa formation (h APF)) onward (Fig. 1e,g and Supplementary Fig. 1a). We found that DCN axons sequentially reach the LP (~36 h APF) and the medulla (~40 h APF) (Fig. 1e,e(i),e(ii)) and stabilize their final adult M-DCN pattern at 44–50 h APF (Fig. 1h, Supplementary Fig. 1b,c and Supplementary Movie 1). We took advantage of imaging intact animals to trace developing axon dynamics within the lobula/LP chiasma (Fig. 1d,d(i),d(ii)). We compared their stable developmental stage (44–50 h APF) with their final adult pattern to identify their final fate (Fig. 1g,h and Supplementary Fig. 1b–d). We found that the final number of M-DCN axons in the chiasma is reached before medulla innervation (40 h APF) (Fig. 1h and Supplementary Fig. 1d). Axons that reached the LP never retracted to the lobula, whereas others retracted without innervating the LP or medulla (Fig. 1h and Supplementary Fig. 1d,e,g). Thus, DCN axon targeting decision is target independent and occurs before future M-DCNs innervate the LP and medulla (~36–40 h APF).

Transient axon amplification correlates with distal innervation

What, if anything, distinguishes future L-DCN from M-DCN axons during development? DCN axons form two transient dynamic structures in the chiasma (Fig. 2a–e and Supplementary Movie 2): single filopodia, which always retract to the lobula (Fig. 2a,b and Supplementary Fig. 1e,g), and transient multi-filopodial structures (Fig. 2a,b,e and Supplementary Fig. 1e,f). Most multi-filopodial structures retract (Fig. 2a), whereas others lead to medulla-innervating axons (Fig. 2a,c, Supplementary Fig. 1e,g and Supplementary Movies 2 and 3). Their structural complexity further decreases (Fig. 2a, Supplementary Fig. 2e), stabilizing, on average, one filopodium (82%) or occasionally two filopodia (18%; hereafter 'bifurcating axons') as a future M-DCN axon (Fig. 2d and Supplementary Fig. 1f(i),h–l). Thus, although a single axonal filopodium is not sufficient to further grow toward the medulla, the formation of transient multi-filopodial structures is a prerequisite (Fig. 2e). Live-imaged DCNs at single-cell resolution in ex vivo brain explants[14] (Fig. 2f–i) revealed that individual axons can amplify to form these multi-filopodial structures (Fig. 2f,h and Supplementary Movie 4), whereas others locally explore the lobula and project unstable individual filopodia into the chiasma (Fig. 2i and Supplementary Movie 5). This indicates an early developmental step controlling transient axonal amplification in the chiasma and maintaining a pool of axons in the lobula.

Spatio-temporal variation in post-mitotic Notch signaling

How are these two axonal behaviors regulated? Live imaging revealed two types of axonal structures in the chiasma that failed to reach the medulla: single filopodium and a subset of amplified axons (Fig. 2e and Supplementary Movie 3). We previously showed that constitutive Notch activation in immature DCNs leads to an absence of medulla innervation in adult brains[11] (Fig. 3j). To gain temporal insight into Notch activity, we monitored the expression of the Notch activity marker E(spl) m7-HLH (m7)[18], using a GFP-tagged m7 protein (m7–GFP) under the control of its endogenous promotor. Between L3 and 50 h APF across fixed individual brains, both the number and proportion of m7^{+} cells within a DCN cluster were highly variable through developmental time and between hemispheres of each individual brain (Fig. 3a–i), with no expression detected after 50 h APF. Thus, post-mitotic Notch signaling is both transient and stochastic during DCN axon targeting.

These data do not formally preclude a pre-existing lineage-based Notch-dependent bias, where hemilineage identity partially

Fig. 1 | DCN targeting decision precedes distal target innervation. (See also Supplementary Fig. 1). **a**,**b**, Single-cell clones (magenta) of L-DCN ($n = 5$ clones; $N = 5$ optic lobes) (**a**, **a(i)**) and M-DCN ($n = 5$ clones; $N = 5$ brains) (**b**, **b(i)**). White star: LP. Arrowhead: lobula (Lo) and medulla (Me) innervations. Yellow arrow (high magnification panel): chiasma. CB, cell bodies. **c**,**d**, Adult DCN innervation path in the optic lobe from dorsal view ($n = 3$ brains) (**c**) and posterior view ($n = 10$ brains) (**d**). **c(ii)**, M-DCN axons cross the chiasma in one plane (yellow arrow) to innervate the LP (black star) and Me. **d(i)**,**(ii)**, M-DCN axons are organized in a fan-like shape along the dorso-ventral axis. Green: DCNs (CD4–tdGFP). Neuropile/N-cadherin (N-Cad, magenta). Cell bodies (DAPI, blue). White arrow: chiasma. **d(ii)**, Cross-section of **d(i)** showing M-DCN axons in the chiasma. **e**–**e(iii)**, Sequential DCN target innervation: Lo, LP (yellow arrow) and Me (blue arrow). **f**, Schematics of intravital imaging settings of the intact pupae. **g**, Intravital live imaging of DCN axon development and the final adult pattern. Green: DCNs (CD4–tdGFP). Medulla targeting structures (gray circle); lobula targeting structures (white circle). The GFP expression in the LP from 28 h APF + 2 h before DCN axon extension, labels non-DC neurons from the LP (representative time-lapse of $n = 3$ optic lobes and $N = 3$ brains) (see also Supplementary Movie 1). **h**, Number of lobula and medulla targeting events through time from live imaging data. Those projecting axonal structures can be in the chiasma (white), contact the LP (gray) or invade the LP (black). Scale bars: 50 µm (**a**,**b**); 30 µm (**d(i)**,**(ii)**); 20 µm (**a(i)**–**b(i)** zoom-in, **c(i)**,**g**). **c(i)**,**d(i)**,**(ii)**,**g**, Of note, the GFP in the lobula labeled mainly the ipsilateral innervating dendrites from DCNs together with the contralateral L-DCN axons.

https://doi.org/10.1038/s41593-025-01937-y

preconfigures one of the two fates[19,20]. In the larval central nervous system, neuroblasts asymmetrically divide to self-renew and produce a secondary precursor called ganglion mother cell (GMC). Those GMCs terminally divide into two immature neurons with distinct Notch activities inherited from birth, referred to as Notch^{ON} and Notch^{OFF} hemilineages[21]. The bHLH-O protein Hey is transiently expressed in Notch^{ON} newborn neurons[22]. To investigate whether Notch^{ON}-derived DCNs originate from a Hey^{+} neuronal population, we used a Hey–GFP reporter[22] (Supplementary Fig. 2a). Additionally, we assessed *Hey* expression developmental history using a memory cassette[20] that marks Hey^{+} hemilineage identity in adult (Supplementary Fig. 2b,c). Distinct heminileage origins would predict half of the DCN population

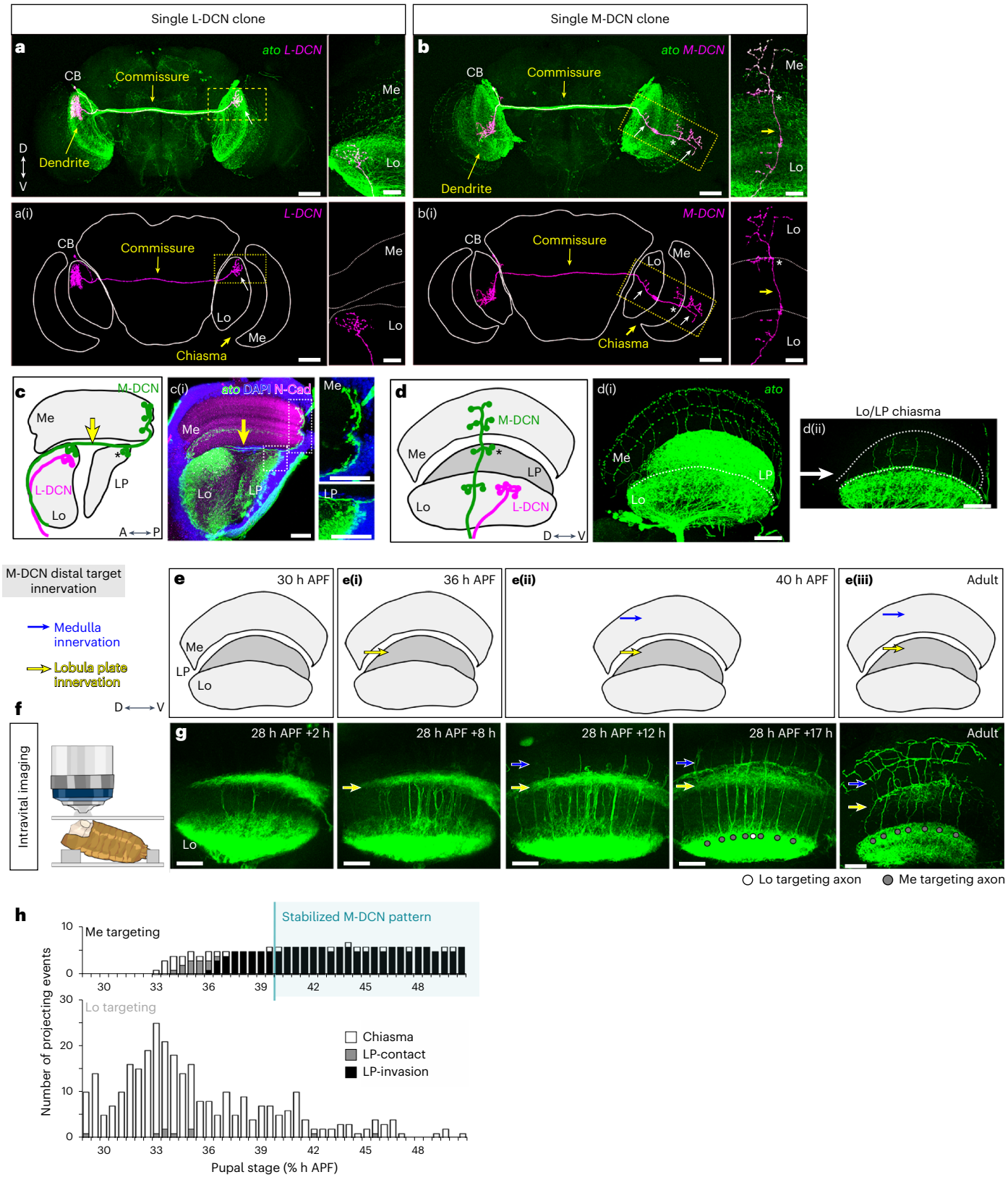

https://doi.org/10.1038/s41593-025-01937-y

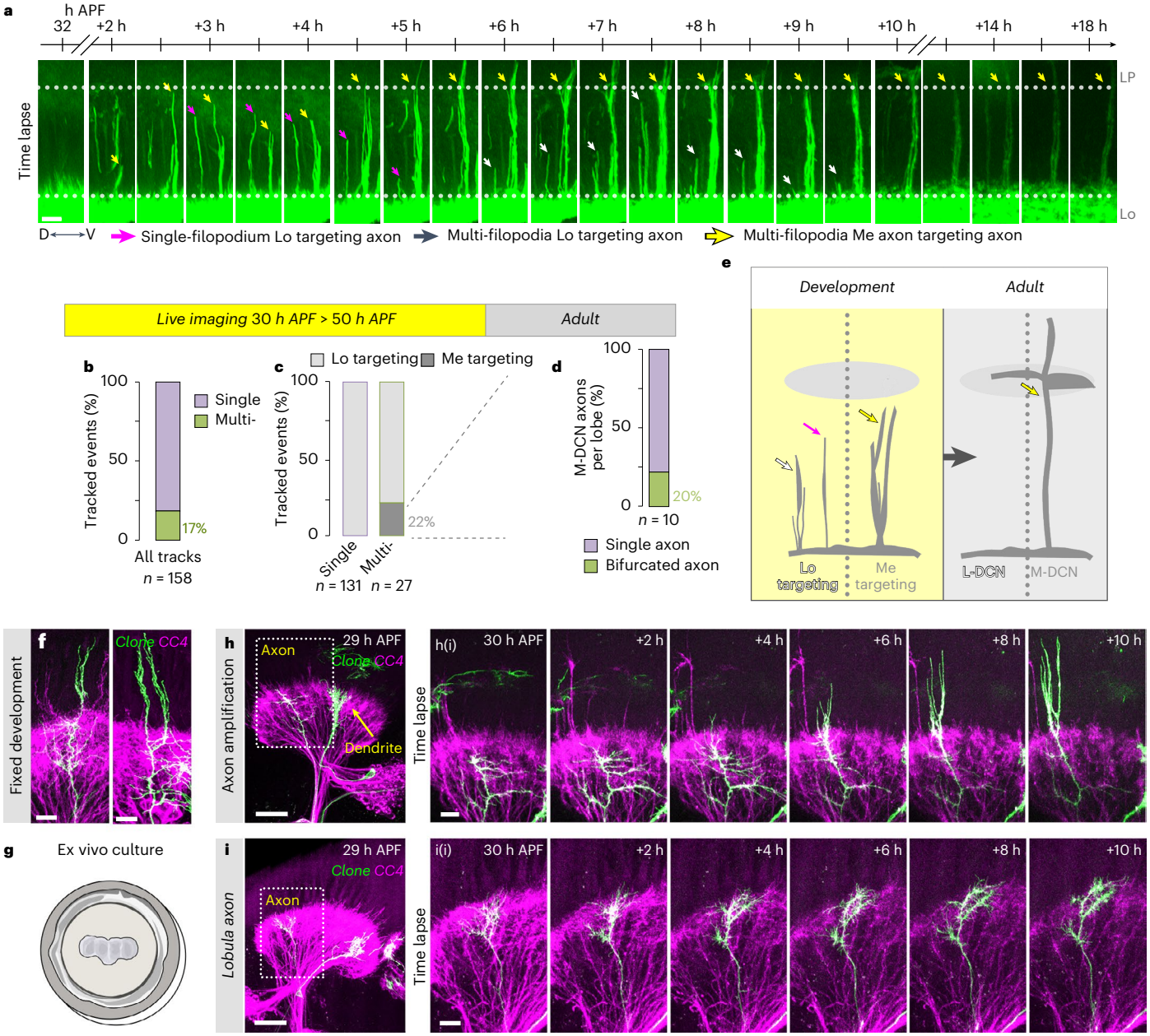

Fig. 2 | Single DCN axons amplify to form multi-filopodial structures that are necessary but not sufficient for medulla targeting. (See also Supplementary Fig. 1). **a**, Representative intravital imaging time-lapse of developing DCN axons projecting in the chiasma from the lobula (Lo) toward the LP ($n = 12$ axonal projection; $N = 2$ brains). Multi-filopodial medulla targeting structures (yellow arrow); single and multi-filopodial lobula targeting structures (magenta and white arrows, respectively). Green: DCNs (CD4–tdGFP) (see also Supplementary Movie 2). **b**–**d**, Proportion of single and multi-filopodial axonal structures projecting in the chiasma. They were tracked over time during intravital live imaging (**b**) and defined a posteriori as medulla or lobula targeting (**c**) based on the final adult pattern (**d**). **e**, DCN multi-filopodial structures correlate with medulla targeting (yellow arrow), whereas both multi and single axonal filopodia structures (white and magenta arrows, respectively) retract to the lobula. **f**, Fixed imaging of a DCN amplifying axon clone (green) at 36 h APF. Magenta: CD4–tdGFP ($n = 11$ clones; $N = 9$ optic lobes). **g**, Schematic of the ex vivo brain culture setup. **h**, Ex vivo live imaging of an amplifying DCN axon clone projecting in the chiasma ($n = 3$; $N = 3$ brains) (see also Supplementary Movie 4). **i**, Ex vivo live imaging of a lobula exploring DCN axon clone ($n = 3$; $N = 3$ brains) (see also Supplementary Movie 5). Green: DCN clone. Magenta: CD4–td. Scale bars: 30 µm (**h**,**i**); 10 µm (**a**,**f**,**h(i)**,**i(i)**).

being Hey$^+$ in L3 and in adult. However, no Hey expression was detected in DCNs using either marker, precluding Notch lineage-based bias. Instead, lineage-independent stochastic variation of Notch signaling temporally overlaps with DCN axon targeting decisions.

Notch signaling temporally restricts axonal amplification

How and when does Notch signaling impact DCN axonal behavior? We expressed an active form of Notch receptor in immature DCNs and tracked axonal structures through development using intravital imaging. Although short individual filopodia still extended into the chiasma from 30 h APF, no multi-filopodial axons were observed, suggesting that Notch activation prevents axon amplification and maintains axons in the lobula (Fig. 3j–l and Supplementary Movie 6). Fixed optic lobe analysis at 36 h APF confirmed this using a marker of future M-DCNs (Supplementary Fig. 2l–q; see later Fig. 5).

We next tested whether Notch activation induces axon retraction. Optogenetic[23] activation of Notch signaling before axons project into the chiasma prevented medulla innervation (Fig. 3m–n,p

and Supplementary Fig. 2d–h). In contrast, activation during or after axon amplification had no effect (Fig. 3m,o–p and Supplementary Fig. 2i–k). To determine whether Notch activation reverts committed M-DCNs into lobula-innervating neurons, we expressed an active form of Notch receptor in committed M-DCNs using a driver expressed in adult M-DCNs but not L-DCNs (VT037804). No L-DCN fate conversions were observed (Supplementary Fig. 2r–s). These results indicate that Notch signaling plays a temporally restricted role in modulating DCN targeting decisions from 0 h APF to 24 h APF, before medulla innervation. Notch activation maintains a pool of axons in the lobula, whereas only Notch^{OFF} DCNs project and amplify in the chiasma. Furthermore, *Notch* knockdown led to more DCN medulla innervation in the adult (Fig. 3q–s) and a corresponding increase in amplified axons at 36 h APF (Fig. 3t–v), without affecting the total number of filopodia per amplified axons (Supplementary Fig. 3a). Thus, lateral inhibition among DCNs defines two subpopulations: Notch^{ON} cells pre-committed to lobula targeting and Notch^{OFF} cells with a non-definite state that project and amplify their axons in the chiasma. Notably, only a subset of Notch^{OFF} cells eventually becomes M-DCNs (Fig. 2a,c), whereas the rest revert to L-DCN morphological fate, indicating that additional developmental steps are required to determine M-DCN identity.

Filopodial dynamics obey an auto-inhibitory feedback rule

Our results indicate that an axon can project one or multiple filopodia in the chiasma (Fig. 2a–e). Although Notch^{OFF} axon amplification correlates with medulla innervation (Fig. 3o–t), the stabilization of a single filopodium in an amplified axon is crucial for medulla innervation and, thus, for the selection of the future M-DCN axon (Fig. 2c–e, Supplementary Fig. 1g and Supplementary Movie 3). To understand the mechanism behind this second specification step, we mathematically described axonal filopodium dynamics by analyzing the distribution of the number of filopodia per axon from live imaging data (Fig. 4a,b and 'Mathematical methods'). At the beginning of chiasma projection (30 h APF) (Fig. 1a,g), the number of filopodia per axon follows a Poisson distribution (with mean $\lambda_1 = 0.84$), suggesting that filopodia grow and retract independently from each other. In contrast, starting at 32 h APF, the distribution gradually deviates from a Poisson distribution (Fig. 4b). Therefore, although filopodial dynamics can be described by a linear birth–death model between 30 h APF and 32 h APF[24], additional parameters likely affect filopodial dynamics afterwards.

We next tested whether the number of filopodia produced by an axon predicts its probability to target the medulla. A statistical independence model (Fig. 4c and 'Mathematical methods') assumes that filopodia act independently, with each having the same probability to stabilize. Thus, the probability of an axon to be selected ($P_{survival(axon)}$) is a function of the probability of a filopodium to become stabilized ($P_{survival(filopodium)}$) and should directly be related to the number of filopodia within an axon. Experimental data showed that axons with five or more filopodia had a high probability to innervate the medulla ($P_{survival(axon)} > 0.60$), whereas those with fewer filopodia rarely became an M-DCN ($P_{survival(axon)} < 0.20$) (Fig. 4c). However, all statistical independence models tested with different probability of a filopodium to stabilize failed to fit experimental data (one-sample Kolmogorov–Smirnov test, 5% significance level, $D > 0.454$ for all models) (Fig. 4c). Thus, a simple increase in filopodia number within an axon is not sufficient to explain its later selection. Instead, the sharp increase in axon selection probability starting from 4–5 filopodia per axon implies the presence of an active regulatory mechanism. We, thus, extended the initial model to include a putative filopodia stabilization process (Fig. 4c,d).

We previously showed that a winner-takes-all model with competition for a limiting resource could explain how stochastic filopodia exploration of *Drosophila* photoreceptors leads to the formation of a restricted number of synapses[25]. We tested whether a similar phenomenon could explain the probability to innervate the medulla (Fig. 4c,d). A winner-takes-all model leads to a low survival probability for axons with fewer than five filopodia, whereas the chance of survival increases rapidly as the number of filopodia increases, reproducing our experimental data (Fig. 4c). This model predicted the final number of stabilized filopodia in adult brains from developmental projecting events in the chiasma, with 84.7% of M-DCNs forming a single medulla axon, whereas 15.3% have a bifurcated axon, consistent with in vivo observations (82–85.0% single, 15.0–18% bifurcated M-DCN axons) (Figs. 2d and 4e and Supplementary Fig. 1h–j). This suggests that a local, cell-intrinsic competitive regulatory mechanism acting between 30 h APF and 33 h APF stabilizes a limited number of filopodia within an amplified axon.

Microtubule growth probabilistically selects distal axons

Filopodia growth and retraction are driven by cytoskeletal dynamics[26]. To gain molecular insight into the selection of a future M-DCN axon, we genetically labeled filamentous actin (F-actin) using Lifeact[27] and microtubules with the alpha-tubulin84B subunit fused with GFP (tubulin–GFP)[28] in DCNs. F-actin was present in all filopodia of an amplified axon (Fig. 5a). In contrast, even though the *alpha-tubulin84B::GFP* construct was expressed using the GAL4/UAS system[29], microtubule levels varied in time and space (Fig. 5b–d, Supplementary Fig. 5a,b and Supplementary Movies 7, 8 and 12). A cytoplasmic-GFP control distributed equally in all filopodia (Supplementary Fig. 4a–c and Supplementary Movies 9–11). An initially thick and stable microtubule network (high intensity, Tub^{GFP+}) at the base of an amplified axon splits within filopodia into a labile network[30] (low intensity, Tub^{GFP-}) that grows, retracts and eventually resorbs (Fig. 5b,d, Supplementary Fig. 5a and Supplementary Movies 7 and 10). Starting at 32 h APF, a stable microtubule (Tub^{GFP+})

Fig. 3 | Notch signaling temporally restricts axonal amplification. (See also Supplementary Figs. 2 and 3). **a**–**f**, Developmental expression of *e(spl)-m7–GFP* Notch reporter (green, blue and yellow arrows) in left and right DCN cluster (magenta) (maximum projection of DCN clusters). **g**–**i**, Number (**g**) and percentage (**h**) of e(spl)-m7–GFP cells (m7$^+$) within DCN clusters. **i**, Left/right paired number of m7$^+$ per cluster and individual brains (one color equals one brain). **j**, Constitutive Notch activation (Notch^{Act}) during DCN development prevents adult medulla (Me) innervation. Green: CD4–tdGFP. Neuropile/N-cadherin (N-Cad, magenta). L3 ($n = 15$, s.d. = 2.9, s.d.% = 4.6); 5 h APF ($n = 6$, s.d. = 2.9, s.d.% = 4.2); 20 hAPF ($n = 8$, s.d. = 2.8, s.d.% = 5.6); 25 h APF ($n = 8$, s.d. = 5.1, s.d.% = 7.3); 30 h APF ($n = 5$, s.d. = 2.2, s.d.% = 3.9); 40 h APF ($n = 4$, s.d. = 2.5, s.d.% = 5.5); 45 h APF ($n = 4$, s.d. = 0.5, s.d.% = 1.6); 50 h APF ($n = 6$, s.d. = 0.90, s.d.% = 0.94). Median, whiskers and interquartile ranges are shown. For detailed statistics, see the 'Statistics and reproducibility' section. **k**, Chiasma view from intravital live imaging of developing DCNs upon Notch^{Act} (time-lapse, $N = 2$ brain observations). White arrowheads: single filopodium (see also Supplementary Movie 6). **l**, Number and length of axon projections over time upon Notch^{Act}, compared to genetic control in Fig. 1h. **m**–**p**, Optogenetic temporal activation of Notch signaling during DCN development and associated adult phenotypes. **m**–**o**, The split LEXA–CRY system was activated through blue light (blue line) to express a constitutive active form of Notch (N^{ICD}) in DCN before (0 h APF to 27 h APF) (**n**) or after (24 h APF to 51 h APF) (**o**) axon amplification. **p**, Quantification of the number of M-DCN axons per adult optic lobes after developmental temporal Notch overactivation. $W = 0$, $P = 0.004624$. **q**–**v**, Downregulation of *Notch* through development impacts medulla innervation. **q**–**s**, Quantification of the number of M-DCN axons per adult optic lobes upon *Notch^{RNAi}* compared to control (Ctrl). $W = 37.5$, $P = 4.851 \times 10^{-5}$. Green: CD4–tdGFP. **t**–**v**, Tracking of the single (blue) and multi (magenta) DCN axonal filopodia in the chiasma at 36 h APF upon *Notch^{RNAi}* compared to control (Ctrl). Green: CD4–tdGFP. **v**, Quantification of the number of multi-filopodial structures (amplified axons) per lobe at 36 h APF in control (Ctrl) versus *Notch^{RNAi}* ($W = 3.5$, $P = 0.0003528$). Scale bars: 30 µm (**j**); 20 µm (**n**,**o**,**q**,**r**,**t**,**u**); 15 µm (**k**); 10 µm (**a**–**f**). **p**,**s**,**v**, All bar plots in these panels show mean and standard error. Two-sided Mann–Whitney *U*-test, (**) $P < 0.01$; (***) $P < 0.001$; (****) $P < 0.0001$.

https://doi.org/10.1038/s41593-025-01937-y

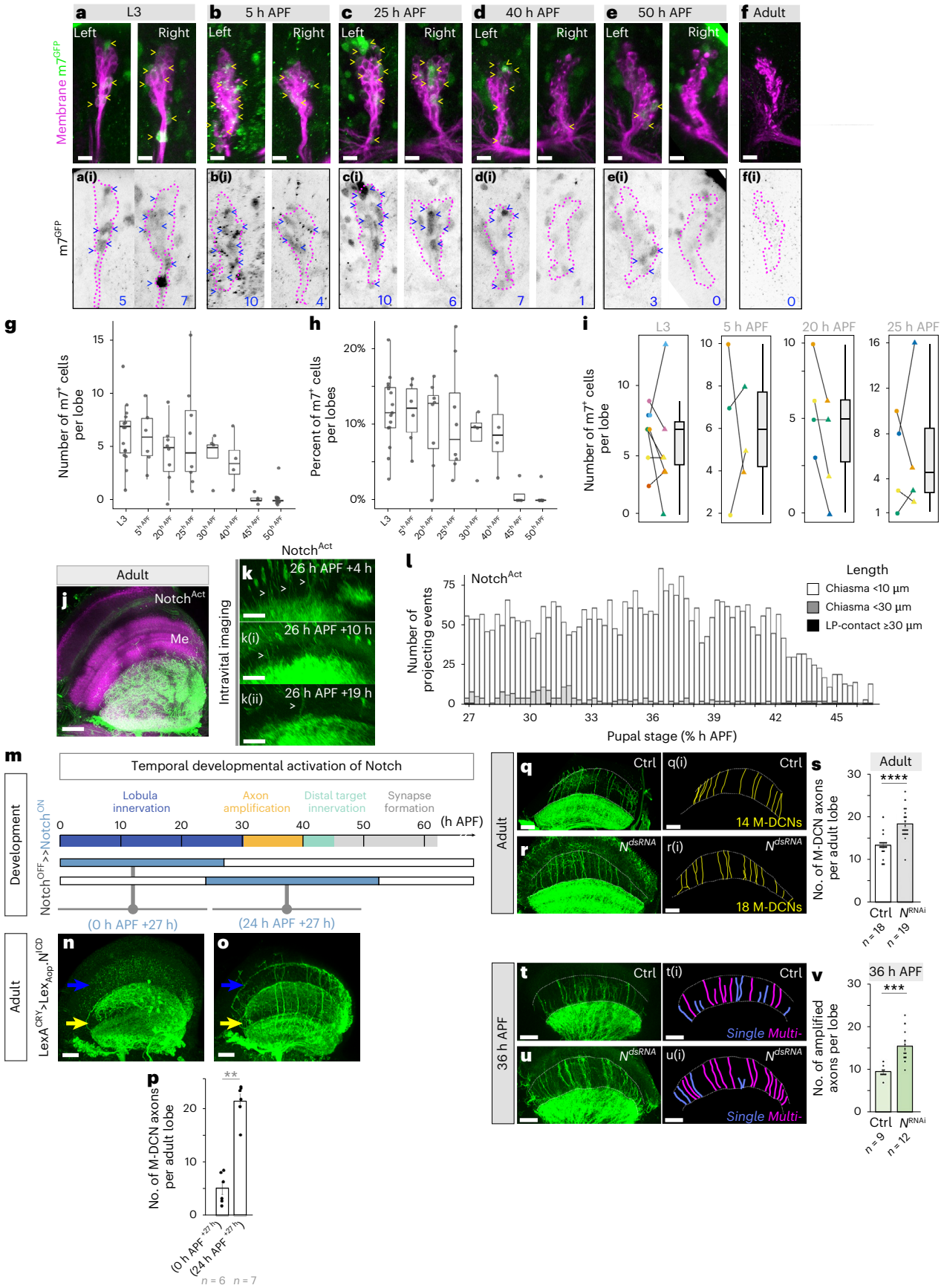

https://doi.org/10.1038/s41593-025-01937-y

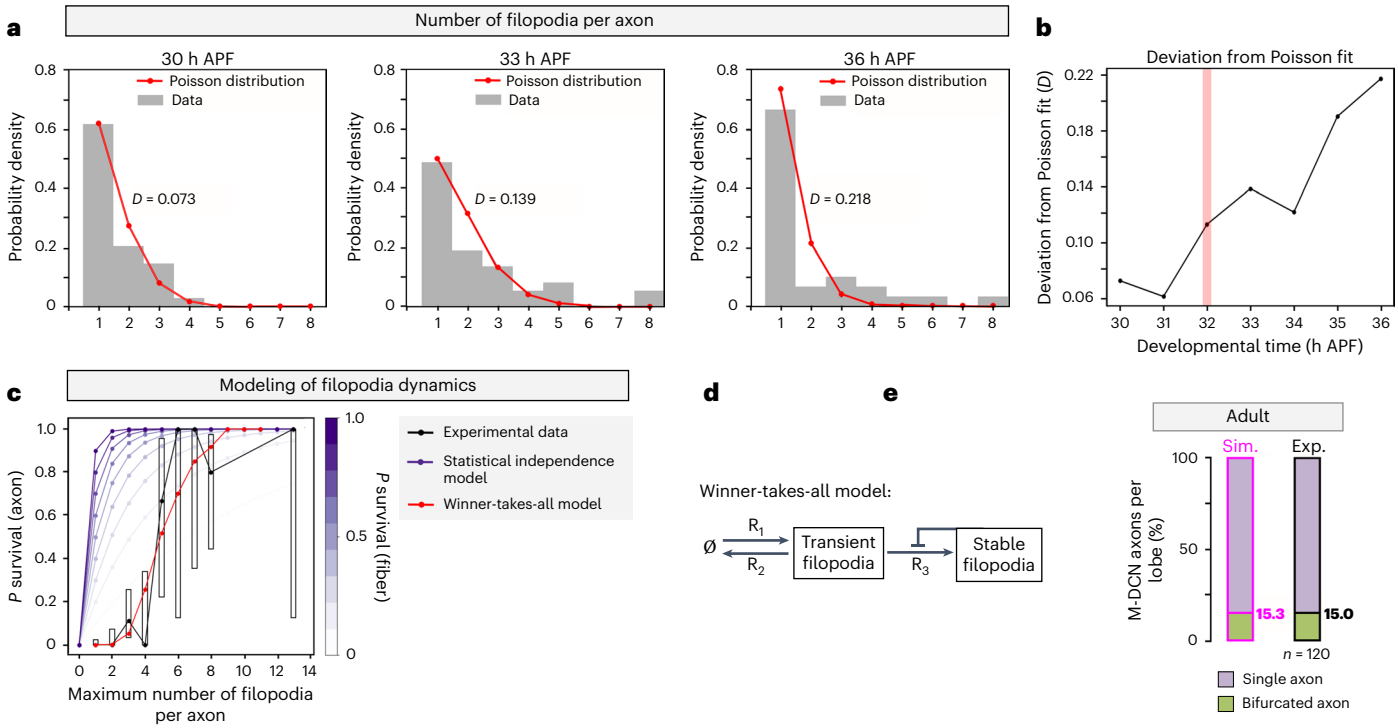

Fig. 4 | An auto-inhibition winner-takes-all feedback model describes DCN axon filopodia dynamics. a,**b**, Filopodia dynamics analysis. **a**, Histogram of the number of filopodia per axon at 30 h APF, 33 h APF and 36 h APF. Gray: experimental data. Red curve: prediction of a Poisson distribution that was fitted to the data. The deviation of the Poisson fit from data was measured by the Kolmogorov–Smirnov distance, *D*. **b**, Deviation from the Poisson fit through time. **c**, Modeling of filopodium dynamics. The probability of axon survival was plottted as a function of the maximum number of filopodia in an axonal structure over time. Gray plot: experimental averages and interquartile ranges of the data. Blue plot: independence model of filopodia in an axonal structure, for a range of filopodium survival probabilities (different brightness levels of the curves). Red plot: simulation average from the 'winner-takes-all' model (50,000 simulations, simulation time of 20 biological hours) with simulation parameters $\kappa = 0.520$, $\delta = 0.535$, $\gamma = 0.08$ and $B_{50} = 4$. **d**, The winner-takes-all model describes the process of the extension, retraction and stabilization of filopodia within a DCN axon in the chiasma and relies on three main reactions: R_1 and R_2, respectively, define the data-derived filopodia extension and retraction parameters, and R_3 introduces the auto-inhibitory dynamics that reduces the chances of a filopodium to become stable (see 'Mathematical methods'). **e**, Simulation of the proportion of adult M-DCNs with one or more filopodia from the winner-takes-all model (50,000 simulations, simulation time of 20 biological hours) compared to fixed experimental data.

network sporadically innervates one or two filopodia, grows and never retracts (Fig. 5b–f, Supplementary Fig. 5c,d and Supplementary Movies 7 and 8). This correlates with when filopodial dynamics deviates from the Poisson distribution (Fig. 4b). Therefore, microtubules stabilize a subset of multi-filopodial axonal structures (Fig. 5f).

Both experimental evidence and computational simulations demonstrate that microtubule stabilization emerges from stochastic growth and collapse dynamics[26,31]. Live imaging of the Tub^{GFP+} network showed a gradual increase in the number of Tub^{GFP+}-labeled filopodia until approximately 36 h APF when it becomes constant, whereas the total filopodia number decreases due to resorption back to the lobula (Fig. 5e,g,h and Supplementary Fig. 5c,d). Finally, the number of stable Tub^{GFP+} filaments at approximately 36 h APF predicts the final M-DCN axon numbers (Fig. 5i–k and Supplementary Fig. 5d), before medulla innervation (40 h APF) (Fig. 1e–g and Supplementary Fig. 1) and synaptogenesis (50 h APF)[32]. Therefore, microtubule stabilization defines a future M-DCN axon. Notably, the probability of an amplified axon to be stabilized by microtubules does not vary along the dorso-ventral axis of the lobula (Fig. 5g,h; two-sided z-test for proportions, all $P > 0.18$), highlighting the stochastic nature of this selection process.

We then tested whether alpha-tubulin84B overexpression could rescue the lack of medulla innervation caused by Notch constitutive activation and found that it did not (Fig. 5l–p and Supplementary Fig. 2l–q). Therefore, microtubule stabilization and Notch signaling act independently at the molecular level. This is consistent with DCNs becoming unresponsive to Notch signaling from 20 h APF, before axon amplification (Fig. 3m–p).

Finally, to test whether microtubule-dependent filopodium stabilization is conserved, we live imaged Atoh1 + dI1 interneurons during floor plate (FP) crossing in chicken embryo spinal cord[33]. Atoh1 + dI1 neurons originate from a common progenitor pool and are post-mitotically determined[34] into two subpopulations that innervate either the ipsilateral or the contralateral ventricular funiculus of the spinal cord. At the FP border, we observed two axon-terminal behaviors. Some terminals contact the FP border, extend and retract short and dynamic axonal protrusions into the FP, to then turn ipsilaterally (Supplementary Movie 13, magenta arrowhead). In contrast, other terminals enter and cross the FP (Supplementary Movie 13, green arrowhead). While crossing the midline, these axon terminals amplify into two branches; one branch later retracts, whereas the other stabilizes and grows (Supplementary Movie 14), a phenomenon reminiscent of *Drosophila* DCN Notch^{OFF} axons in the chiasma. Live imaging of tubulin dynamics in ex vivo intact spinal cords showed that a microtubule network invades both branches and then gradually disappears from one branch before its full retraction, whereas it accumulates and stabilizes the other that continues to grow to become the future dI1c axon (Fig. 5q and Supplementary Movie 15). Thus, like *Drosophila* DCN Notch^{OFF} axons, dI1 interneurons stabilize one branch through a similar microtubule-based process during midline crossing.

Microtubule stoichiometry impacts distal axon selection

Altogether, our observations on labile and stable microtubule dynamics suggest that filopodia within an amplified DCN axon may compete

https://doi.org/10.1038/s41593-025-01937-y

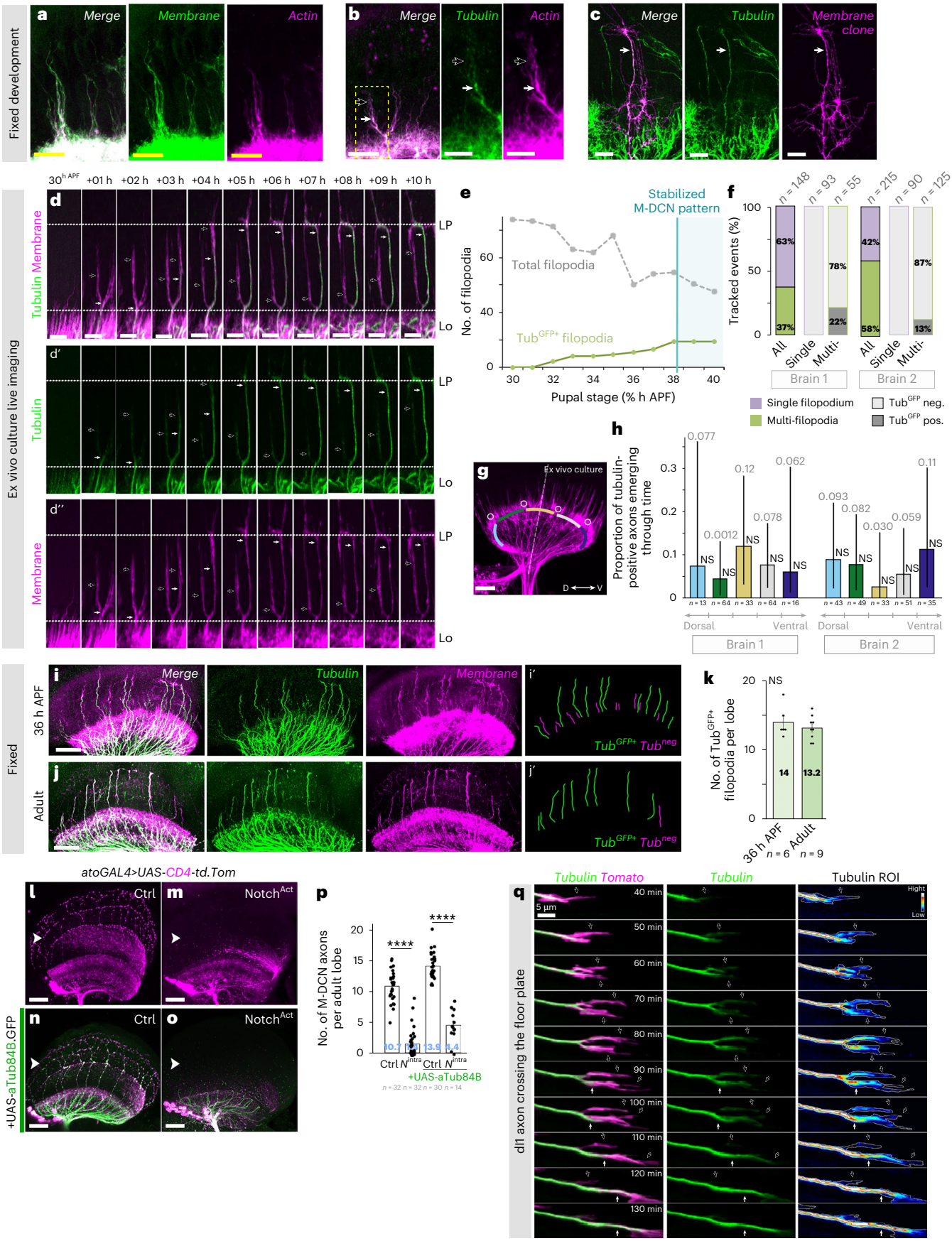

Fig. 5 | Microtubule growth selects future M-DCN axons. (See Supplementary Fig. 5). **a**–**c**, DCN amplifying axons in fixed developing brains. **a**, F-actin (Lifeact, magenta) and membrane (CD4–tdGFP, green). **b**, Two intensity levels of microtubules (green): high (white arrow) and low (black arrow). F-actin (Lifeact, magenta). **c**, Single-cell clone of an amplifying DCN axon (magenta). Tubulin filaments (green, white arrow). **d**, Ex vivo live imaging of a DCN amplified axon with growing microtubule filaments (green, white arrow) (Supplementary Movie 7) and a low amount of dynamic microtubules (black arrow). Membrane: magenta. **e**, Quantification of the number of axonal filopodia and tubulin filaments (Tub^{GFP+}) over time per chiasma. **f**, Proportion of single (purple) and multi-filopodial (green) axonal structures in the chiasma that are stabilized (dark gray) or not (light gray) by microtubules. **g**,**h**, Quantification of the proportion (stated above the bars) of axonal structures with tubulin filaments as a function of space across the lobula. Data are split into five spatial bins from dorsal to ventral (see **h**). 95% confidence intervals (black error bars) were estimated by the Clopper–Pearson method. All pairwise comparisons are not significant (NS, two-sided z-test for proportions, all $P > 0.18$). **i**–**k**, Quantification of the number of microtubule filaments (green) per chiasma at 36 h APF (**i**–**i(i)**,**k**) and in adult (**j**–**j(i)**,**k**). Bar plots show mean and standard error. Two-sided Mann–Whitney *U*-test ($W = 23$, $P = 0.6733$). **l**–**p**, Alpha-tubulin84B overexpression upon Notch constitutive activation ($Notch^{Act}$). Membrane (CD4–tdTomato, magenta); tubulin (GFP, green). **p**, Quantification of the number of M-DCN axons per adult optic lobes. Bar plots show mean and standard error. Kruskal–Wallis test, chi-squared = 87.521, df = 3, $P = 2.2 \times 10^{-16}$ (for exact Dunn test *P* values, see the 'Statistics and reproducibility' section), (****) $P < 0.0001$. **q**, Live imaging of tubulin (green) in transient dI1 axon growth cone splitting crossing the midline. Tubulin–GFP appears at low intensity (black arrowhead), accumulates in the stabilized branch (white arrowhead) and resorbs in the retracting one. Magenta: tdTomato-F. Heat map shows tubulin intensity: Hi, high; Lo, low. Time-lapse of $n = 3$ observations, $N = 3$ animals (see Supplementary Movie 15). Scale bars: 10 µm (**a**–**c**); 5 µm (**b** zoom-in,**k**); 20 µm (**d**,**i**); 30 µm (**f**,**g**,**k**–**n**). ROI, region of interest.

for microtubule resources (Fig. 6a–a(i)), explaining the winner-takes-all distribution (Fig. 4c). We tested whether our model could predict the number of M-DCN axons in the *UAS-alphaTubulin84B::GFP* background, previously used to visualize microtubules and estimate filopodial dynamics. Our live imaging data showed that 8.1% of filopodial projection led to a Tub^{GFP+} marked axon and, hence, a selected axon (Fig. 6b). In fixed adult brains, we observed an average of 12.7 M-DCN axons per optic lobes (Fig. 6d and Supplementary Fig. 6a,b). Similarly, our simulations estimated that 7.9% of developmental projection events are selected (Fig. 6b), generating an average of 12.2 M-DCN axons per adult optic lobes (Fig. 6c, red bar). We further compared the simulated outcome of a gradual decrease in the stabilization rate parameter γ, which mimics the reduction of a limiting stabilization factor (Fig. 6c and 'Mathematical methods'), to the effect of a downregulation of tubulin elements using RNA interference (RNAi) against different *Drosophila* alpha-tubulin isotypes[35]: alpha1 (alphaTub84B), alpha2 (alphaTub85E) or alpha3 (alphaTub84D) in developing post-mitotic DCNs (Fig. 6d–h). Both led to fewer M-DCN axons in adult (Fig. 6c,d). Overexpression of alpha-tubulin84B in developing DCNs did increase medulla innervation (Fig. 6d and Supplementary Fig. 6a,b) and rescued the different alpha-tubulin isotype knockdowns (Fig. 6d–l). Therefore, alpha-tubulin level, but not isotype specificity, is critical for axonal targeting. Notably, tubulin overexpression did not substantially affect the number and the percentage of bifurcated M-DCN axons (Supplementary Fig. 6c,d), supporting the notion that tubulin levels mainly regulate the probability of a single filopodium to be stabilized within each multi-filopodial structure. Therefore, tubulin acts as a limiting resource in the selection of future M-DCNs (Fig. 6a–a(i)), and additional factors may regulate the asymmetric stabilization of microtubules.

Differential microtubule flow reveals asymmetric instability

To identify the molecular process underlying this asymmetric microtubule polymerization in amplified axons, we first examined the distribution of the microtubule plus-end binding protein EB1 as a read-out of microtubule polymerization using EB1–GFP[36]. Its distribution fluctuates between filopodia (Fig. 6m,n(i), Supplementary Fig. 7 and Supplementary Movies 16 and 17), even when stable tubulin starts to accumulate in amplified axons (32–34 h APF) (Fig. 5e). Thus, EB1 distribution alone does not predict future microtubule stabilization in a single filopodium. However, we did observe asymmetric EB1–GFP dynamics: EB1–GFP moved toward the axon tip of some filopodia, whereas others exhibited bidirectional flow, suggesting microtubule instability in non-stable filopodia (Fig. 6n). This differential microtubule flow may drive asymmetric tubulin stabilization.

Changes in microtubule flow and orientation are critical for axon specification in primary cultured neurons[37]. In *Drosophila*, the actin–microtubule crosslinker Spectraplakin ACF7/Short Stop (Shot) regulates axonal growth, cargo transport and microtubule biogenesis[38–40]. During DCN axon selection, Shot protein isoforms ($Shot^{LA}$ and $Shot^{LC}$) initially localize at the base of several filopodia in an amplified axon in agreement with previous Shot localization observations[40] but, later, asymmetrically accumulate in a single filopodium (Fig. 6o–r). Both *shot* knockdown and overexpression led to an increase in the initial number of amplified axons at 36 h APF (Fig. 6s–u,y–z). In contrast, *shot* knockdown reduced adult M-DCN axons (Fig. 6v–t,AA,AB), indicating that Shot is essential for filopodial selection but not initial formation. Furthermore, *shot* overexpression increased both selected and bifurcated axons (Fig. 6u,x,AA,AB). Therefore, Shot is a regulator of asymmetric microtubule stabilization.

Fig. 6 | Tubulin acts as a limiting resource in the selection of future M-DCNs. (See Supplementary Figs. 6 and 7). **a**–**a(i)**, Winner-takes-all biological model (Fig. 4d). **a**, 30–32 h APF: actin-rich filopodia stochastically extend (R_1) and retract (R_2) in the chiasma. **a(i)**, At 32 h APF, microtubule-based stabilization changes global filopodium dynamics with tubulin as a limiting resource for filopodium stabilization. Five or more filopodia axons show higher microtubule stabilization probability per filopodium (R_3), restricting stabilization material in neighboring filopodia. **b**, Prediction of the proportion of axonal projection events (tracked axons) in the chiasma leading to medulla or lobula targeting recapitulates experimental observations of microtubule-stabilized axons (Tub^{GFP+}). **c**, Number of adult M-DCN axons predicted per optic lobes when decreasing the stabilization rate parameter γ, mimicking limiting stabilization factor reduction. **d**, Quantification of adult M-DCN axons in the chiasma upon a developmental alpha-tubulin84B overexpression (yellow, $W = 144.5$, $P = 0.02331$) (**d(i)**), alpha-tubulin isotype downregulation (gray, chi-squared = 27.6905, df = 3, $P = 0$) (**d(ii)**) or alpha-tubulin isotype downregulation in an alpha-tubulin84B overexpression background (green, chi-squared = 1.75, df = 3, $P = 0.6259$) (**d(iii)**). **e**–**l**, Effect of developmental alpha-tubulin downregulation monomers on adult medulla innervation (**e**–**h**) and its rescue by alpha-tubulin84B isotype overexpression (**i**–**l**). **m**–**n(i)**, EB1–GFP ex vivo live imaging in DCN amplified axon (Supplementary Movie 16). **n**–**n(i)**, Kymographs showing anterograde (**n**) and anterograde/retrograde (**n(i)**) movement of EB1. **o**–**r**, Localization of Shot-LC^{GFP} (**o**,**p**) or Shot-LA^{GFP} (**q**,**r**) proteins in amplified axons. Fixed brain. Membrane: magenta; Shot: green. Scale, 10 µm (**s**–**x**) *shot* knockdown ($shot^{RNAi}$) or overexpression ($UAS\text{-}shot^{LC}$) impact on single filopodium (blue) and amplified axon (magenta) formation at 36 h APF (**s**–**u**) and on adult medulla innervation (**v**–**x**). **y**–**AB**, Quantification of the number of amplified axons (chi-squared = 9.1171, df = 2, $P = 0.01048$) (**y**) and filopodia (chi-squared = 8.7343, df = 2, $P = 0.01269$) (**z**) per lobe at 36 h APF and number of adult M-DCN axons (chi-squared = 39.452, df = 2, $P = 2.71 \times 10^{-9}$) (**AA**) and bifurcated axons (chi-squared = 5.6277, df = 2, $P = 0.05997$) (**AB**). **d(i)**, Two-sided Mann–Whitney *U*-test; **d(i)**,**(ii)**,**Y**–**AB**, Kruskal–Wallis test (for exact Dunn test *P* values, see the 'Statistics and reproducibility' section). **m**,**p**, Two-sided Mann–Whitney *U*-test, (*) $P < 0.05$; (**) $P < 0.01$; (***) $P < 0.001$; (****) $P < 0.0001$. All bar plots of the panels show mean and standard error. Scale bars, 10 µm (**o**–**r**); 20 µm (**s**–**u**); 30 µm (**e**–**l**,**v**–**x**).

https://doi.org/10.1038/s41593-025-01937-y

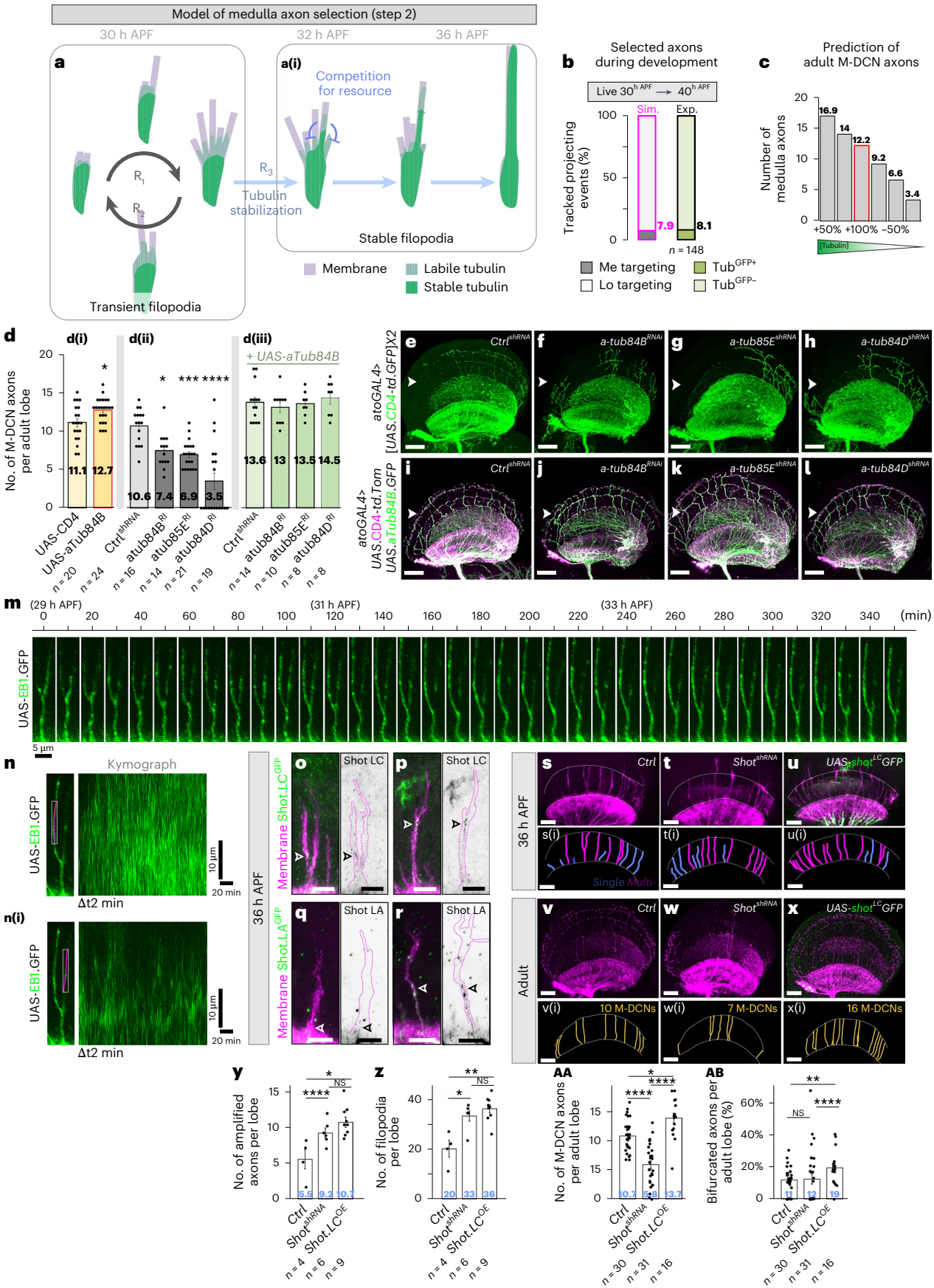

https://doi.org/10.1038/s41593-025-01937-y

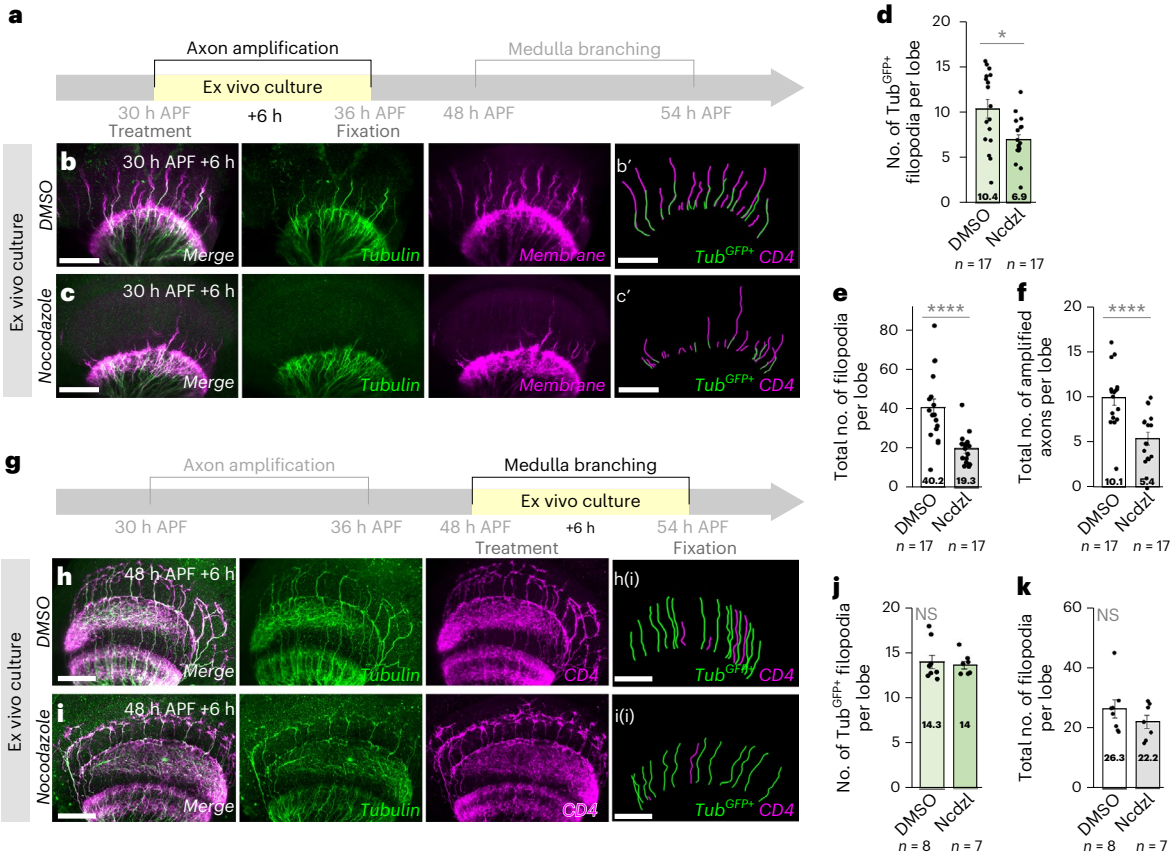

Fig. 7 | Microtubule stabilization selects future M-DCNs during a specific developmental critical period. (See also Supplementary Fig. 8). **a**–**c**, Ex vivo cultured brains treated with Nocodazole (Ncdzl) or DMSO from 30 h AFP to 36 h APF during axon extension in the chiasma. Quantification of the number of tubulin filaments ($W = 216$, $P = 0.01403$) (**d**), the total number of filopodia per lobe ($W = 257$, $P = 0.000113$) (**e**) and the number of amplified axons in the chiasma in control (DMSO) versus Nocodazole treatment ($W = 249$, $P = 0.0003074$) (**f**). **g**–**i**, Ex vivo cultured brains treated with Nocodazole or DMSO after M-DCN pattern stabilization from 48 h APF. Quantification of the number of tubulin filaments (**j**) and the total number of filopodia per lobe in the chiasma in control (DMSO) versus Nocodazole treatment (**k**). Scale bars: 30 µm (**a**–**c(i)**,**h**–**i(i)**). Green: tubulin. Magenta: membrane (CD4–tdGFP). Bar plots show mean and standard error. Two-sided Mann–Whitney *U*-test, (****) $P < 0.0001$.

A microtubule stabilization developmental critical period

Finally, to identify the temporal window of microtubule stabilization, we treated ex vivo cultured brains with Nocodazole—a drug known to bind free tubulin dimers[41]—during axon amplification (30–36 h APF) (Fig. 7a–f and Supplementary Fig. 8). This treatment reduced Tub^{GFP+} filaments as well as the total number of filopodia and amplified axons in the chiasma (Fig. 7d–f, Supplementary Fig. 8 and Supplementary Movies 18 and 19), indicating impaired axon selection. However, Nocodazole treatment after the final M-DCN pattern stabilization (48 h APF) had no effect on M-DCN axon number, suggesting that microtubule-based axon selection is irreversible after this point (Fig. 7g–l). Therefore, during a critical developmental period, filopodia within an amplified axon compete to establish a stable microtubule network, determining the future M-DCN axon.

Discussion

Our work explores the developmental origin of individual morphological variation in adult brain wiring. In the fly visual system, DCN/LC14 wiring varies between left and right hemispheres and among isogenic flies[11], leading to individualized object response behavior[3]. This variation relies on differential innervation of proximal (lobula) versus distal (medulla) optic lobe neuropiles by DCN axons. We previously showed that medulla innervation probability involves a Notch cell-based competition among post-mitotic immature DCNs and is not instructed by lineage-inherited factors[11]. Our current work reveals two successive stochastic developmental decisions distinct in space and time that progressively restrict DCN potential to innervate the medulla. Initially, while DCN axons innervate the lobula, a stochastic Notch activation (Notch^{ON}) retains most axons proximally, whereas Notch^{OFF} status permits the formation of transient amplifying structures in the chiasma. In a subsequent Notch-independent step, microtubules stabilize 1–2 filopodia within some Notch^{OFF} amplified axons through intra-neuronal competition, whereas axons that fail to stabilize a filopodium collapse. The statistical distribution of 0–2 stabilized filopodia within a neuron underscores the probabilistic nature of this underlying selection process. This leads to medulla innervation by a small subset of DCN axons that, thus, become M-DCNs.

Early Notch activation was sufficient to instruct L-DCN fate, hence preventing M-DCN formation, but did not retract amplified axons or reverse M-DCN commitment. Axon development involves multiple signals that modulate immature neuron intrinsic states until a final state is reached[42]. JNK signaling acts downstream of Notch to impact DCN medulla innervation potential[11] and is modulated by Wnt and FGF signaling[43]. We imagine that, as a DCN axon explores its microenvironment, it also navigates its intrinsic temporal states. Sequential spatial and temporal activation of local signals such as Wnt and FGF may drive potential changes in chromatin accessibility as shown in the developing mouse cortex[44], rendering DCNs non-responsive to further Notch activation. This would explain why specific signals can act only in specific temporal windows.

During the second phase of medulla targeting, we showed that Notch^{OFF} DCN axons amplify into several long parallel actin-rich

https://doi.org/10.1038/s41593-025-01937-y

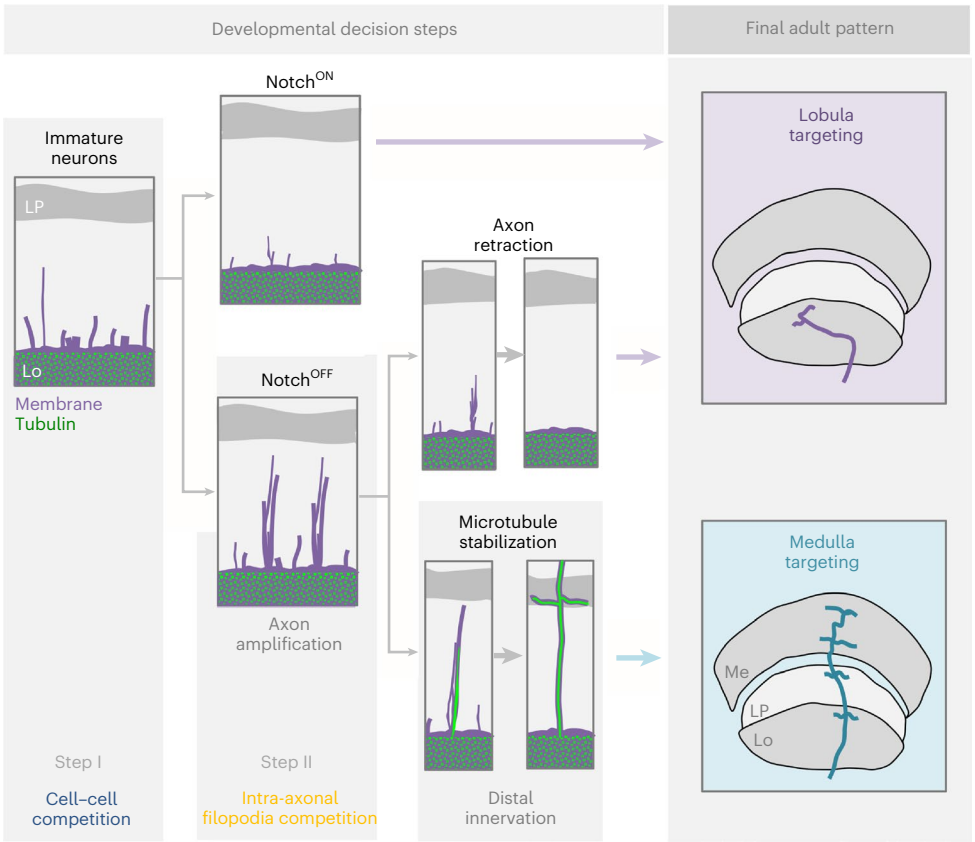

Fig. 8 | Model. A developmental succession of probabilistic steps creates individualized axonal wiring patterns. First, Notch lateral inhibition between immature post-mitotic DCNs defines a pool of axons that stay in the lobula ($Notch^{ON}$), whereas $Notch^{OFF}$ axons project in the chiasma with an intermediate undefined fate. The second selection step relies on the capacity for the remaining $Notch^{OFF}$ DCNs to amplify to form multi-filopodial structures. A competitive microtubule-dependent process then stabilizes 1–2 filopodia from an amplifying axon—a future M-DCN axon shaft—whereas an absence of microtubule leads to a collapse to the lobula. Lo, lobula; Me, medulla.

filopodia generated from single cells. This phenomenon extends beyond DCNs[33,45,46]; chicken dI1 axons transiently amplify while crossing the spinal cord FP[33], and mouse corticospinal axons form filopodia-like extensions when navigating into the basilar pons[46]. Such conserved growth cone behavior may arise from spatial confinement or a change in substrate, when growth cones migrate from a dense neuropile to a sparser environment organized into open channels[47,48]. This radical change in morphology could also reflect a bet-hedging strategy as a growth cone crosses less adhesive environments, whereby the extension of multiple long parallel filopodia in the same direction would increase the probability of at least one filopodium reaching a more adhesive target[49]. We found that amplified DCN axons with more than five long filopodia have a significant chance to stabilize and cross the optic chiasma. However, the sole increase in filopodia number does not recapitulate the axon selection process, arguing against a simple bet-hedging model.

Our model predicts that filopodia within an amplified axon intrinsically compete for resources that drive microtubule growth and stabilization. Within an axon, filopodia share a common pool of tubulin elements and regulatory proteins at the labile microtubule domain, between the actin-rich filopodia and axon shaft (stable microtubule). As supported by our EB1 data, microtubule dynamic instability occurs in these regions[30] and can be influenced by cell compartment volume or free tubulin concentration[50,51]. Axons with fewer than five filopodia may lack the critical concentration required for microtubule assembly. Conversely, more filopodia would expand axonal subcellular volume, providing more stable microtubule nucleation sites[52], therefore promoting growth. This would also generate local fluctuation of free tubulin and building block components[50], leading to competition for a limiting resource and, thus, a winner-takes-all scenario. As a result, each axon would act as an autonomous agent, making a local targeting decision. Notably, altering alpha-tubulin monomer expression impacts M-DCN selection, whereas overexpression still results in stabilization of 1–2 filopodia per axons. Thus, tubulin serves as a permissive factor for filopodia stabilization[53], predicting involvement of microtubule-regulating factors.

We identified Short Stop (Shot), a Spectraplakin protein, as a regulator of asymmetric stable microtubule localization during DCN axon selection. Although Shot enrichment in axon shaft and single filopodium of amplified axons would suggest a potential role in microtubule stabilization, its presence at the base of filopodia is reminiscent of its known role in microtubule organization[38,39]. In that context, an attractive model is that Shot regulates microtubule orientation among filopodia in DCN amplified axons. This would send an asymmetric signal that affects catastrophe rate[54], promoting selective microtubule stabilization in a single filopodium, priming it for M-DCN fate. In agreement with this scenario, loss of *shot* function reduces filopodia stabilization. More notably, our data suggest that distinct microtubule regulatory mechanisms operate during DCN axon selection. Our Nocodazole experiment (Fig. 7) suggests that microtubule polymerization can affect either the formation or the dynamics of transient filopodia, similarly to what has been observed during initial axon extension in cultured neurons[55]. The dynamically unstable nature of microtubules, along with actin network regulators[43], would mechanistically reflect the R_1–R_2 reactions of our mathematical model (Fig. 6a). Second, increased axonal amplification during development followed by reduced adult M-DCNs upon *shot* knockdown (Fig. 6s–ab) suggests that axons without Shot can generate but fail to stabilize transient filopodia, reflecting the R_3 reaction of our

model. Although our work addressed cell-intrinsic and axon-intrinsic mechanisms that result in stereotypic growth patterns, we speculate that these mechanisms are influenced by extrinsic factors such as Wnt and FGF, previously identified as potential sources of the regulation of extrinsic axon targeting[43]. Future work will elucidate the link between intrinsic and extrinsic mechanisms.

Finally, like *Drosophila* DCNs, we showed that dI1 contralateral interneurons in the chick spinal cord amplify and then stabilize one branch through a probabilistic microtubule-based process while crossing the midline. This suggests that both Notch^{OFF} DCN axons and dI1 axons rely on a conserved stochastic targeting process. Like DCNs, dI1 neurons originate from a common progenitor pool and are divided into two subpopulations, namely the ipsilateral (dI1i) and the contralateral (dI1c)[34], with distinct innervation sites. Although extracellular molecules influence dI1 axon targeting[42], further investigation will shed light on whether and how Notch post-mitotically specifies dI1 subtypes. dI1i and dI1c determinants and markers are dynamically expressed during dI1 development[34,56]. Together with our study, this highlights the importance of addressing the spatio-temporal dynamic aspects of developmental processes to understand how neurons generated from the same progenitor diverge over time.

Overall, our work supports a model (Fig. 8) whereby final innervation patterns, and, thus, the stabilization of neuronal terminal fate, cannot be predicted from cell birth. Instead, a final wiring pattern emerges gradually in each brain through iterative algorithmic growth, where the output of each developmental step provides the input for the subsequent, but mechanistically independent, step. Perhaps most remarkably, we found that the final innervation pattern is variable across individual brains and cannot be precisely predicted from the mechanism but must, instead, be observed live until it is stabilized, consistent with the most salient prediction of the concept of wiring by algorithmic growth[57].

Online content

Any methods, additional references, Nature Portfolio reporting summaries, source data, extended data, supplementary information, acknowledgements, peer review information; details of author contributions and competing interests; and statements of data and code availability are available at https://doi.org/10.1038/s41593-025-01937-y.

References

1. Schlegel, P. et al. Information flow, cell types and stereotypy in a full olfactory connectome. *eLife* **10**, e66018 (2021).
2. Pascual, A., Huang, K.-L., Neveu, J. & Préat, T. Brain asymmetry and long-term memory. *Nature* **427**, 605–606 (2004).
3. Linneweber, G. A. et al. A neurodevelopmental origin of behavioral individuality in the *Drosophila* visual system. *Science* **367**, 1112–1119 (2020).
4. Chou, Y. H. et al. Diversity and wiring variability of olfactory local interneurons in the *Drosophila* antennal lobe. *Nat. Neurosci.* **13**, 439–449 (2010).
5. Mitchell, K. J. Developmental noise is an overlooked contributor to innate variation in psychological traits. *Behav. Brain Sci.* **45**, e171 (2022).
6. Honegger, K. & de Bivort, B. Stochasticity, individuality and behavior. *Curr. Biol.* **28**, R8–R12 (2018).
7. Hiesinger, P. R. & Hassan, B. A. The evolution of variability and robustness in neural development. *Trends Neurosci.* **41**, 577–586 (2018).
8. Waddington, C. H. Canalization of development and the inheritance of acquired characters. *Nature* **150**, 563–565 (1942).
9. Rihani, K. & Sachse, S. Shedding light on inter-individual variability of olfactory circuits in *Drosophila*. *Front. Behav. Neurosci.* **16**, 835680 (2022).
10. Smith, M. A. Y., Honegger, K. S., Turner, G. & De Bivort, B. Idiosyncratic learning performance in flies. *Biol. Lett.* **18**, 20210424 (2022).
11. Langen, M. et al. Mutual inhibition among postmitotic neurons regulates robustness of brain wiring in *Drosophila*. *eLife* **2**, e00337 (2013).
12. Hassan, B. A. et al. Atonal regulates neurite arborization but does not act as a proneural gene in the *Drosophila* brain. *Neuron* **25**, 549–561 (2000).
13. Zheng, X. et al. Baboon/dSmad2 TGF-β signaling is required during late larval stage for development of adult-specific neurons. *EMBO J.* **25**, 615–627 (2006).
14. Özel, M. N., Langen, M., Hassan, B. A. & Hiesinger, P. R. Filopodial dynamics and growth cone stabilization in *Drosophila* visual circuit development. *eLife* **4**, e10721 (2015).
15. Langen, M. et al. The developmental rules of neural superposition in *Drosophila*. *Cell* **162**, 120–133 (2015).
16. Jukam, D. & Desplan, C. Binary fate decisions in differentiating neurons. *Curr. Opin. Neurobiol.* **20**, 6–13 (2010).
17. Agi, E., Kulkarni, A. & Hiesinger, P. R. Neuronal strategies for meeting the right partner during brain wiring. *Curr. Opin. Neurobiol.* **63**, 1–8 (2020).
18. Couturier, L., Mazouni, K., Corson, F. & Schweisguth, F. Regulation of Notch output dynamics via specific E(spl)-HLH factors during bristle patterning in *Drosophila*. *Nat. Commun.* **10**, 3486 (2019).
19. Lee, Y. J. et al. Conservation and divergence of related neuronal lineages in the *Drosophila* central brain. *eLife* **9**, e53518 (2020).
20. Mark, B. A developmental framework linking neurogenesis and circuit formation in the *Drosophila* CNS. *eLife* **10**, e67510 (2021).
21. Truman, J. W., Moats, W., Altman, J., Marin, E. C. & Williams, D. W. Role of Notch signaling in establishing the hemilineages of secondary neurons in *Drosophila melanogaster*. *Development* **137**, 53–61 (2010).
22. Monastirioti, M. et al. *Drosophila* Hey is a target of Notch in asymmetric divisions during embryonic and larval neurogenesis. *Development* **137**, 191–201 (2010).
23. Chan, Y. B., Alekseyenko, O. V. & Kravitz, E. A. Optogenetic control of gene expression in *Drosophila*. *PLoS ONE* **10**, e0138181 (2015).
24. Gadgil, C., Chang, H. L. & Othmer, H. G. A stochastic analysis of first-order reaction networks. *Bull. Math. Biol.* **67**, 901–946 (2005).
25. Özel, M. N. et al. Serial synapse formation through filopodial competition for synaptic seeding factors. *Dev. Cell* **50**, 447–461 (2019).
26. Lawrence, E. J., Chatterjee, S. & Zanic, M. More is different: reconstituting complexity in microtubule regulation. *J. Biol. Chem.* **299**, 105398 (2023).
27. Riedl, J. et al. Lifeact: a versatile marker to visualize F-actin. *Nat. Methods* **5**, 605–607 (2008).
28. Grieder, N. C., de Cuevas, M. & Spradling, A. C. The fusome organizes the microtubule network during oocyte differentiation in *Drosophila*. *Development* **127**, 4253–4264 (2000).
29. Brand, A. H. & Perrimon, N. Targeted gene expression as a means of altering cell fates and generating dominant phenotypes. *Development* **118**, 401–415 (1993).
30. Baas, P. W., Rao, A. N., Matamoros, A. J. & Leo, L. Stability properties of neuronal microtubules. *Cytoskeleton (Hoboken)* **73**, 442–460 (2016).
31. Tang, Q. et al. Interplay between stochastic enzyme activity and microtubule stability drives detyrosination enrichment on microtubule subsets. *Curr. Biol.* **33**, 5169–5184 (2023).
32. Dutta, S. B., Linneweber, G. A., Andriatsilavo, M., Hiesinger, P. R. & Hassan, B. A. EGFR-dependent suppression of synaptic autophagy is required for neuronal circuit development. *Curr. Biol.* **33**, 517–532 (2023).

33. Dumoulin, A., Zuñiga, N. R. & Stoeckli, E. T. Axon guidance at the spinal cord midline—a live imaging perspective. *J. Comp. Neurol.* **529**, 2517–2538 (2021).
34. Wilson, S. I., Shafer, B., Lee, K. J. & Dodd, J. A molecular program for contralateral trajectory: Rig-1 control by LIM homeodomain transcription factors. *Neuron* **59**, 413–424 (2008).
35. Gasic, I. Regulation of tubulin gene expression: from isotype identity to functional specialization. *Front. Cell Dev. Biol.* **10**, 898076 (2022).
36. Rogers, S. L., Rogers, G. C., Sharp, D. J. & Vale, R. D. *Drosophila* EB1 is important for proper assembly, dynamics, and positioning of the mitotic spindle. *J. Cell Biol.* **158**, 873–884 (2002).
37. Burute, M., Jansen, K. I., Mihajlovic, M., Vermonden, T. & Kapitein, L. C. Local changes in microtubule network mobility instruct neuronal polarization and axon specification. *Sci. Adv.* **8**, eabo2343 (2022).
38. Sun, T. et al. Spectraplakin Shot maintains perinuclear microtubule organization in *Drosophila* polyploid cells. *Dev. Cell* **49**, 731–747 (2019).
39. Lu, W., Lakonishok, M. & Gelfand, V. I. Gatekeeper function for Short stop at the ring canals of the *Drosophila* ovary. *Curr. Biol.* **31**, 3207–3220 (2021).
40. Sanchez-Soriano, N. et al. Mouse ACF7 and *Drosophila* Short stop modulate filopodia formation and microtubule organisation during neuronal growth. *J. Cell Sci.* **122**, 2534–2542 (2009).
41. Hoebeke, J., Van Nijen, G. & De Brabander, M. Interaction of oncodazole (R 17934), a new anti-tumoral drug, with rat brain tubulin. *Biochem. Biophys. Res. Commun.* **69**, 319–324 (1976).
42. Stoeckli, E. T. Understanding axon guidance: are we nearly there yet? *Development* **145**, dev151415 (2018).
43. Srahna, M. et al. A signaling network for patterning of neuronal connectivity in the *Drosophila* brain. *PLoS Biol.* **4**, e348 (2006).
44. van den Ameele, J. et al. Reduced chromatin accessibility correlates with resistance to Notch activation. *Nat. Commun.* **13**, 2210 (2022).
45. Li, T. et al. Cellular bases of olfactory circuit assembly revealed by systematic time-lapse imaging. *Cell* **184**, 5107–5121 (2021).
46. Bastmeyer, M. & O'Leary, D. D. M. Dynamics of target recognition by interstitial axon branching along developing cortical axons. *J. Neurosci.* **16**, 1450–1459 (1996).
47. Jang, K. J. et al. Two distinct filopodia populations at the growth cone allow to sense nanotopographical extracellular matrix cues to guide neurite outgrowth. *PLoS ONE* **5**, e15966 (2010).
48. Villard, C. Spatial confinement: a spur for axonal growth. *Semin. Cell Dev. Biol.* **140**, 54–62 (2023).
49. Turney, S. G. et al. Variation and selection in axon navigation through microtubuledependent stepwise growth cone advance. Preprint at *bioRxiv* https://doi.org/10.1101/2020.01.29.925602 (2020).
50. Janulevicius, A., Van Pelt, J. & Van Ooyen, A. Compartment volume influences microtubule dynamic instability: a model study. *Biophys. J.* **90**, 788–798 (2006).
51. Hjorth, J. J. J., Van Pelt, J., Mansvelder, H. D. & Van Ooyen, A. Competitive dynamics during resource-driven neurite outgrowth. *PLoS ONE* **9**, e86741 (2014).
52. Jonasson, E. M. et al. Behaviors of individual microtubules and microtubule populations relative to critical concentrations: dynamic instability occurs when critical concentrations are driven apart by nucleotide hydrolysis. *Mol. Biol. Cell* **31**, 589–618 (2020).
53. Kiss, A., Fischer, I., Kleele, T., Misgeld, T. & Propst, F. Neuronal growth cone size-dependent and -independent parameters of microtubule polymerization. *Front. Cell. Neurosci.* **12**, 195 (2018).
54. Jakobs, M. A. H., Zemel, A. & Franze, K. Unrestrained growth of correctly oriented microtubules instructs axonal microtubule orientation. *eLife* **11**, e77608 (2022).
55. Zhao, B. et al. Microtubules modulate F-actin dynamics during neuronal polarization. *Sci. Rep.* **7**, 9583 (2017).
56. Tulloch, A. J., Teo, S., Carvajal, B. V., Tessier-Lavigne, M. & Jaworski, A. Diverse spinal commissural neuron populations revealed by fate mapping and molecular profiling using a novel *Robo3*^{Cre} mouse. *J. Comp. Neurol.* **527**, 2948–2972 (2019).
57. Hiesinger, P. R. *The Self-Assembling Brain*. https://doi.org/10.2307/j.ctv191kwz2 (2021).

Methods

Fly stocks and experiments

For all experiments, pupae were aged at 25 °C, and female *D. melanogaster* were selected at 0 h APF (white pupae) based on the absence of male gonads. The following fly stocks were used: *ato.14A-GAL4* (BDSC#6480)[12], UAS-*CD4-tdGFP* on 2nd and 3rd chromosomes (BDSC#35839 and BDSC#35836)[58], *UAS-CD4-tdTomato* (III) (BDSC#35837)[58], *pBPhsFlp2::PEST* (X)[59], *UAS-FRT-STOP-FRT.CD4-tdGFP*, hey-GFP.FPTB (III) (BDSC#64826), [*Hey:T2A:FLP, UAS-myr:GFP, UAS-FRT-STOP-FRT-myr:sfGdP:HA*] (gift from the Doe laboratory)[20], $[e(spl)\text{-}C\text{-}GFPm7]_{BAC}$ (gift from the Schweisguth laboratory)[18], *UAS-Notch*^{dsRNA} (BDSC#7077), *UAS-Notch*$^{intra.GS}$ (BDSC#52008)[60], *lexAop-Notch*^{intra}[61], *UAS-CIBN::LexA-mcherry-p65::CRY2* (gift from the Kravitz laboratory)[23], *UAS-LifeAct.RFP*[27] (III) (BDSC#58362), *UAS-Lifeact-Ruby*[27] (II) (BDSC#35545), *UASp-GFPS65C-alphaTub84B* on 2nd and 3rd chromosomes (BDSC#7374 and BDSC#7373)[28], *UAS-EGFP* (X) (BDSC#5428), *pBPhsFlp2::PEST;;10UAS-HA_V5_FLAG*[59], UAS-EB1-GFP[36] (III) (BDSC#35512), shRNA control (VDRC#60200), UAS-tub84B RNAi (VDRC#33427), UAS-tub84D RNAi (VDRC#330509), UAS-tub85E RNAi (VDRC#330369), UAS-shot.L(C)GFP (BDSC#29042), UAS-shot.L(A)GFP (BDSC#29044) and UAS-shot shRNA (VDRC#330586).

Genotypes

The list of genotypes for all figures and supplementary material:

Figure 1
Figure 1a–b: pBPhsFlp2::PEST in attP3/w; +/+; ato.14 A.GAL4, UAS-CD4.td-GFP/ pJFRC201-10XUAS-FRT > STOP > FRT-myr::smGFP-HA in VK0005, pJFRC240-10XUASFRT > STOP > FRT-myr::smGFP-V5-THS-10XUAS-FRT > STOP > FRT-myr::smGFP-FLAG
Figure 1c–d, g–h: w/w; UAS-CD4.td-GFP /+; ato.14 A.GAL4, UAS-CD4.td-GFP /+

Figure 2
Figure 2a–d: w/w; UAS-CD4.td-GFP /+; ato.14 A.GAL4, UAS-CD4.td-GFP
Figure 2f: pBPhsFlp2::PEST in attP3/w; +/+; ato.14 A.GAL4, UAS-CD4.td-GFP/ pJFRC201-10XUAS-FRT > STOP > FRT-myr::smGFP-HA in VK0005, pJFRC240-10XUASFRT > STOP > FRT-myr::smGFP-V5-THS-10XUAS-FRT > STOP > FRT-myr::smGFP-FLAG
Figure 2h–i: pBPhsFlp2::PEST in attP3/w; UAS-FRT > STOP > FRT-CD4.td-GFP/+; ato.14 A.GAL4, UAS-CD4.td-Tomato/+

Figure 3
Figure 3a–i: w/w; $[e(spl)\text{-}C\text{-}GFPm7]_{BAC}$ /+; ato.14 A.GAL4, UAS-CD4.td-Tomato
Figure 3j–l: w/w; UAS-Notch$^{intra.GS}$/+; ato.14 A.GAL4, UAS-CD4.td-GFP /+
Figure 3m–p: w/w; LexAop-Notch^{intra} /UAS-CD4.td-GFP; ato.14 A.GAL4, UAS-CIBN::LexA-mcherry-p65::CRY2/+
Figure 3c,e: w/w; + /+; ato.14 A.GAL4, UAS-CD4.td-Tomato, UAS-CIBN::LexA-mcherry-p65::CRY2/+
Figure 3q,s,t,v: w/w; +/+; ato.14 A.GAL4, UAS-CD4.td-GFP / +
Figure 3r,s,u,v: w/w; +/+; ato.14 A.GAL4, UAS-CD4.td-GFP / UAS-Notch$^{dsRNA\#7077}$

Figure 4
Figure 4a–b, e: w/w; UASp-GFPS65C-alphaTub84B /+; ato.14 A.GAL4, UAS-CD4.td-Tomato /+

Figure 5
Figure 5a: w/w; UAS-Lifeact-Ruby/+; ato.14 A.GAL4, UAS-CD4.td-GFP /+
Figure 5b: w/w; UASp-GFPS65C-alphaTub84B /+; ato.14 A.GAL4/ UAS-LifeAct.RFP/+
Figure 5c: pBPhsFlp2::PEST in attP3/w; UASp-GFPS65C-alphaTub84B /+; ato.14 A.GAL4/ pJFRC201-10XUAS-FRT > STOP > FRT-myr::smGFP-HA, pJFRC240-10XUASFRT > STOP > FRT-myr::smGFP-V5-THS-10XUAS-FRT > STOP > FRT-myr::smGFP-FLAG
Figure 5d–k: w/w; UASp-GFPS65C-alphaTub84B /+; ato.14 A.GAL4, UAS-CD4.td-Tomato/+
Figures 5l,5p: w/w; + /+; ato.14 A.GAL4, UAS-CD4.td-Tomato/+
Figures 5n,5p: w/w; UAS-Notch$^{intra.GS}$ /+; ato.14 A.GAL4, UAS-CD4.td-Tomato/+
Figure 5o,p: w/w; UASp-GFPS65C-alphaTub84B / UAS-Notch$^{intra.GS}$; ato.14 A.GAL4, UAS-CD4.td-Tomato/+

Figure 6
Figure 6d(i): w/w; +/+; ato.14 A.GAL4, UAS-CD4.td-Tomato/+
Figure 6b,d(i): w/w; UASp-GFPS65C-alphaTub84B /+; ato.14 A.GAL4, UAS-CD4.td-Tomato/+
Figure 6d(ii),e: w/w; UAS-CD4.td-GFP / P{VDRCsh60200}attP40; ato.14 A.GAL4, UAS-CD4.td-GFP/ +
Figure 6d(ii),f: w/w; UAS-CD4.td-GFP /+; ato.14 A.GAL4, UAS-CD4.td-GFP/ P{aTub84B RNAi.GD9679}v33427
Figure 6d(ii),g: *w/w; UAS-CD4.td-GFP/P{aTub85E shRNA VSH330369} attP40; ato.14 A.GAL4, UAS-CD4.td-GFP*
Figure 6d(ii),h: w/w; UAS-CD4.td-GFP / P{ aTub84D shRNA VSH330509}attP40; ato.14 A.GAL4, UAS-CD4.td-GFP
Figure 6d(iii),i: w/w; UASp-GFPS65C-alphaTub84B/P{VDRCsh60200} attP40; ato.14 A.GAL4, UAS-CD4.td-Tomato / +
Figure 6d(iii),j: w/w; UASp-GFPS65C-alphaTub84B /+; ato.14 A.GAL4, UAS-CD4.td-Tomato / P{aTub84B RNAi.GD9679}v33427
Figure 6d(iii),k: w/w; UASp-GFPS65C-alphaTub84B / P{ aTub85E shRNA VSH330369}attP40; ato.14 A.GAL4, UAS-CD4.td-Tomato
Figure 6d(iii),l: w/w; UASp-GFPS65C-alphaTub84B / P{ aTub84D shRNA VSH330509}attP40; ato.14 A.GAL4, UAS-CD4.td-Tomato
Figure 6m–n(i): w/w;+/+; UAS-EB1-GFP /ato.14 A.GAL4, UAS-CD4.td-Tomato
Figure 6o–p, **U,X, Y–AB**: w/w; UAS-shotL(C)-GFP /+; ato.14 A.GAL4, UAS-CD4.td-Tomato/+
Figure 6q–r: UAS-shotL(A)-GFP /w; +/+; ato.14 A.GAL4, UAS-CD4.td-Tomato/+
Figure 6t,w, **Y–AB**: w/w; UAS-shot^{shRNA} /+; ato.14 A.GAL4, UAS-CD4.td-Tomato/+
Figure 6s,v, **Y–AB**: w/w; UAS-shot^{shRNA} /+; ato.14 A.GAL4, UAS-CD4.td-Tomato/+

Figure 7
Fig. A–K: w/w; UASp-GFPS65C-alphaTub84B /+; ato.14 A.GAL4, UAS-CD4.td-Tomato/+

Supplementary Figures:
Fig.1a-h: w/w; UAS-CD4.td-GFP /+; ato.14 A.GAL4, UAS-CD4.td-GFP / +
Fig. 2a: w/w; +/+; hey-GFP.FPTB / ato.14 A.GAL4, UAS-CD4.td-Tomato
Fig. 2b–c: w/w; +/+; Hey:T2A:FLP, UAS-myr:GFP, UAS-FRT-STOP-FRT-myr:sfGdP:HA / ato.14 A.GAL4
Fig. 2d, f: w/w; +/+; ato.14 A.GAL4, UAS-CD4.td-Tomato, UAS-CIBN::LexA-mcherry-p65::CRY2/+
Fig. 2d, g–k: w/w; LexAop-Notch^{intra} /+; ato.14 A.GAL4, UAS-CD4.td-Tomato, UAS-CIBN::LexA-mcherry-p65::CRY2/+
Fig. 2l: w/w; UASp-GFPS65C-alphaTub84B /+; ato.14 A.GAL4, UAS-CD4.td-Tomato/+
Fig. 2m: w/w; UASp-GFPS65C-alphaTub84B /+; ato.14 A.GAL4, UAS-CD4.td-Tomato/ UAS-Notch$^{intra.GS}$
Fig. 2r: w/w; +/+; VT037804.GAL4, UAS-CD4.td-GFP /+
Fig. 2s: w/w; +/+; VT037804.GAL4, UAS-CD4.td-GFP / UAS-Notch$^{intra.GS}$
Fig. 3a: w/w; +/+; ato.14 A.GAL4, UAS-CD4.td-GFP /+
w/w; +/+; ato.14.GAL4, UAS-CD4.td-GFP / UAS-Notch$^{dsRNA\#7077}$
Fig. 4a: UAS-EGFP / w; +/+; ato.14 A.GAL4, UAS-CD4.td-Tomato
Fig. 5a–d: w/w; UASp-GFPS65C-alphaTub84B /+; ato.14 A.GAL4, UAS-CD4.td-Tomato

Fig. 6a, c–d: w/w; + /+; ato.14 A.GAL4, UAS-CD4.td-Tomato
Fig. 6b, c–d; S6B–E: w/w; UASp-GFPS65C-alphaTub84B /+; ato.14 A.GAL4, UAS-CD4.td-Tomato
Fig. 7a: w/w;+/+; UAS-EB1-GFP /ato.14 A.GAL4, UAS-CD4.td-Tomato
Fig. 8: w/w; UASp-GFPS65C-alphaTub84B /+; ato.14 A.GAL4, UAS-CD4.td-Tomato

Movies:
Movie 1–3: w/w; +/+; ato.14 A.GAL4, UAS-CD4.td-GFP / +
Movie 4, 5: pBPhsFlp2::PEST in attP3/w; UAS-FRT > STOP > FRT-CD4.td-GFP/+; ato.14 A.GAL4, UAS-CD4.td-Tomato/+
Movie 6: w/w; UAS-Notch$^{intra.GS}$/+; ato.14 A.GAL4, UAS-CD4.td-GFP /+
Movie 7–8–10–16–17: w/w; UASp-GFPS65C-alphaTub84B /+; ato.14 A.GAL4, UAS-CD4.td-Tomato
Movie 9: UAS-EGFP / w; +/+; ato.14 A.GAL4, UAS-CD4.td-Tomato
Movie 14, 15: w/w;+/+; UAS-EB1-GFP /ato.14 A.GAL4, UAS-CD4.td-Tomato

Clonal induction

To induce multi-color flip-out (MCFO)[59] clone for fixed analysis (Figs. 1a,b and 2f) and CD4–tdGFP flip-out clone induction for live imaging (Fig. 2h,i), white pupae were collected and heat shocked for 15 min at 37 °C, and then grown until the indicated developmental age or adulthood.

Temporal optogenetic activation of Notch

We used the *UAS-LEXA.CRY* system[23] to control the expression of the Notch receptor intracellular domain (NICD). The split LEXA–p65 transcription factor (TF) is expressed in the DCN under the control of the ato14A.GAL4 driver and is inactive in dark. Upon blue light exposure, the CIBN/CRY system reconstitutes a functional LEXA–p65 TF, which activates the transcription of NICD.

Fly crosses were kept in dark at 25 °C. Female F1 white pupae (0 h APF) were collected under red light and raised in dark at 25 °C until the indicated timepoint of blue light exposure. For optogenetic induction, pupae were transferred to a vial and exposed to constant blue light (Blue LED, tension 24 V, from LED-motion, ref. 6302) for the indicated duration and then put back into dark at 25 °C, with the following parameters: photons per surface unit per second: $Np = 3.5 \times 10^{17}$ photons m^{-2} s^{-1}; irradiance: $I = 1.5 \times 10^{-12}$ W m^{-2}; wavelength: 470 nm.

Immunostaining and fixed imaging

Immunostaining was done for all the fixed datasets. Pupal and adult brains were dissected in PBS and fixed 20 min in 3.7% paraformaldehyde (PFA). Washes were done in PBS, 0.4% Triton-X (PBST). Antibody incubations were performed in PBST and normal donkey serum 1:200 (Sigma-Aldrich, S30-100ML) overnight at 4 °C for primary antibodies and for 3 h at room temperature for secondary antibodies. Samples were mounted in VECTASHIELD (Vector Laboratories) and imaged using a ×63 glycerol objective (numerical aperture (NA) = 1.3) with a Leica TCS SP8-X white laser confocal microscope.

Antibodies. The following antibodies were used: anti-GFP (chicken; Abcam, ab13970; 1:500), anti-mCherry (rabbit; Abcam, ab167453; 1:500) or anti-DsRed (rabbit; ClonTech; 1:300) to stain against Tomato, anti-N-cadherin (rat monoclonal; Developmental Studies Hybridoma Bank; DN-Ex 8; 1:50), anti-Flag DYKDDDDK Epitope (rat monoclonal; Novus Biologicals, NBP1-067-12 clone L5; 1:200), anti-HA (rabbit monoclonal; Cell Signaling Technology, C29F4; 1:300), anti-V5 clone SV5-Pk4 (mouse monoclonal; Bio-Rad, MCA1360; 1:500), Alexa Fluor 488 AffiniPure donkey anti-chicken IgY (IgG) (H + L) (1:500; Jackson ImmunoResearch, 703-545-155, AB_2340375), Alexa Fluor 647 AffiniPure donkey anti-rat IgG (H + L) (1:500; Jackson ImmunoResearch, 712-605-153, RRID: AB_2340694), Cy3 AffiniPure donkey anti-mouse IgG (H + L) (1:500; Jackson ImmunoResearch, 715-165-151, RRID: AB_2315777), DyLight 405 AffiniPure donkey anti-rabbit IgG (H + L) (1:500, Jackson ImmunoResearch, 711-475-152, RRID: AB_2340616), Cy3 AffiniPure donkey anti-rabbit IgG (H + L) (1:500; Jackson ImmunoResearch, 711-165-152, RRID: AB_2307443) and Alexa Fluor 488 AffiniPure donkey anti-goat IgG (H + L) (1:500; Jackson ImmunoResearch, 705-545-003, RRID: AB_2340428).

Drosophila intravital mounting

Pupae expressing two copies of the *UAS-CD4.td-GFP* transgene under the control of the promoter *ato14A-GAL4* (ref. 12) were staged and aged at 25 °C from 0 h APF until the indicated hour for imaging. The cuticle surrounding the pupal head was then removed. Pupae were mounted by following the protocol described in Langen et al.[15] to image the DCNs through the right eye. To compare the developing and adult DCN patterns from the same brain, pupae were then removed from the chamber after imaging and kept at 25 °C until adulthood. The corresponding 1-week-old adults were dissected, fixed and stained for further confocal imaging.

Drosophila brain culture

Ex vivo *Drosophila* brain cultures were performed according to the methods described by Ozel et al.[14] using 0.4% low-melting agarose and Schneider's culture medium supplemented with 20-hydroxyecdysone (1 µg ml^{-1} final) (Sigma-Aldrich, 5289-74-7), insulin HUMAN (10 µg ml^{-1} final) (Gibco, 12585014), penicillin–streptomycin (1:100) (Gibco, 15140122) and FBS (1:10) (Gibco, 16141-061). Pupal brains were dissected 1 h before the imaging timepoint in Schneider's *Drosophila* Medium. Two layers of 1 × 1-mm squares of 200-mm tape were used as spacers.

Nocodazole treatment

Pupal brains were dissected in Schneider's *Drosophila* Medium 30 min before the indicated timepoint (30 h APF or 48 h APF) of drug treatment and embedded at the indicated timepoint into 0.4% low-melting agarose in culture medium (see Ozel et al.[14]) further complemented with 10 µg ml^{-1} (33 µM) final concentration of Nocodazole (Sigma-Aldrich, SML1665-1ML) or DMSO (Sigma-Aldrich, D8418-50ML). Embedded brains were then kept at 25 °C in DMSO or Nocodazole supplemented culture medium for 6 h. After treatment, brains were removed from the low-melted agarose and fixed and immuno-stained as described above. For ex vivo live imaging, brains in low-melted agarose were mounted as the regular protocol with drug-supplemented culture medium and were imaged 30 min to 1 h after the drugs were added.

Live imaging acquisitions (*Drosophila*)

Drosophila live imaging experiments were performed at 25 °C and acquired on a Leica SP8 MP two-photon microscope with a ×40 IRAPO water objective (NA = 1.1), a Chameleon Ti:Sapphire laser and a resonant scanner with a single excitation laser at 896 nm for one-color imaging (GFP) or at 920 nm for two-color imaging (GFP/Tomato). Intravital imaging parameters were as follows: image resolution: 1,024 × 1,024; resonant scanner, laser power: 40%; gain: 40%. Ex vivo imaging parameters were as follows: image resolution: 1,024 × 1,024; resonant scanner, laser power: 5%; gain: 40%, dwell time: 0.8 µs.

The Nocodazole and EB1–GFP ex vivo live imaging experiments were acquired on an Ultima 2Pplus Bruker two-photon microscope with an N20X-PFH ×20 Olympus XLUMPLFLN objective (NA = 1.00, 2.0 mm working distance (WD)) and a 920-nm excitation laser (image resolution: 1,024 × 1,024; galvo scanner, laser power: 120%; dwell time: 0.8 µs).

Live imaging acquisition benchmarking (*Drosophila*)

(See 'Mathematical methods'). The targeting process we are following takes over 20 h from 30 h APF to 50 h APF. Intravital live imaging necessitates imaging the total z-stack (~200 stacks) of approximately 300 µm over more than 24 h, where an entire imaged individual develops and is kept until adulthood. This allowed us to intravital live image with a frame

rate of 30 min, in absence of photobleaching or damaged sample, as we discarded all recordings of animals that did not develop into adults. With these parameters, we were able to discriminate between single filopodium that always remain single and single filopodia that would further contact other filopodia through time to form multi-filopodia structures. More notably, we could identify that the key structures to follow and, thus, to benchmark are the multi-filopodia axons (Fig. 2a). Using ex vivo live imaging with a 20-min frame rate and intravital imaging with a 30-min frame rate, we analyzed the likelihood of a multi-filopodia structure to have a lifespan under our timescale (20–30 min) and found that 85% and 82%, respectively, of the observed multi-filopodia structures have a longer lifespan of 20 min or more (Supplementary Fig. 9c,d). Although we cannot rule out that there is a second population of fast and dynamic multi-filopodia transient structures, we are confident that our imaging captures the vast majority of these events. Of note, in the current setup, we are focusing on the projecting events rather than the axon identity itself, meaning that transient single filopodia can originate from the same axon. Second, we estimate the power of detection of the multi-filopodia structures according to different frame rates (Supplementary Fig. 9e,f). With a 40-min frame rate, approximately 88% of the multi-filopodia structures can be detected, in conditions that do not damage our samples. Reducing by twice the frame rate from 40 min to 20 min only increases the proportion of detected multi-filopodia structures by 7–10%. Therefore, we consider that our intravital 30-min frame rate is sufficient to capture the projection of multiple filopodia structures—key events of distal axon targeting.

Image processing and analysis

Images were processed and analyzed on Imaris 10.1.0 (2023 Nov 15) (Bitplane). During pupal development, the optic lobe undergoes a global rotation during the first half of the metamorphosis[62]. Similarly, the medulla rotates and is pulled by the lamina from 25 h APF[15,63]. These rotations could be observed during our in vivo intravital live imaging and were corrected using the 'Image Alignement' module from Imaris. The Imaris oblique-slice tool was used to visualize the DCN axon in the chiasma area. Removal of the non-specific background for Fig. 6i–l in the green channel was performed based on the DCN CD4–td.Tomato channel (magenta) using the Imaris mask option. To quantify the number of total axons (single and multi-filopodia), the number of filopodia, the percentage of amplified axons and the number of filopodia per axons for our fixed dataset and each timepoint of our four-dimensional datasets, axonal structures in the lobula/LP chiasma were skeletonized using the 'Filament Tracer' module from Imaris. During development, an axonal structure was defined as 'multi-filopodia' (that is, an amplified axon) when two or more filopodia shared at least one contact point. To track axonal structures through time, which refers to a 'projecting event', we used the 'TrackingLineage' module from Imaris. To quantify the number of M-DCN axons in adult, each 'Filament' was counted as an axon regardless of shared contact point. To quantify the number and percentage of 'bifurcated' axons in adult, we defined 'bifurcated' axons group of 'filaments' that share a contact point. The percentage of 'bifurcated' axons was, thus, quantified over the sum of single and grouped 'filaments' within an optic lobe. A tracked axonal structure was identified as tubulin–GFP positive (Tub^{GFP+}) if it showed a continuous and similar level of tubulin–GFP labeling as its axon shaft (where stable tubulin proteins are located). Figures were assembled using Adobe Photoshop 2022 (23.0.0 release).

Notch activity quantification

Enhancer-of-split (*E(spl)*) genes are well-characterized direct targets of Notch[64–68]. Although we previously identified that the E(spl)mbeta-CD2 reporter was expressed in a DCN subset at 32 h APF, it showed a weak expression. We, therefore, used the E(spl)m7–GFP Notch reporter[18,69] that showed a strong GFP signal in one copy, which allowed robust and accurate quantification. Using immunostaining against GFP, we analyzed each DCN cell body cluster through z-stacks using Fiji: we defined a two-dimensional area of interest on stacks centered on the cell body for each DCN of a cluster. Cells showing intense GFP signal were scored as 'Notch positive'.

In ovo electroporation

We used a plasmid encoding membrane-bound farnesylated td-Tomato (td-Tomato-F) under the control of the Math1 enhancer and the β-globin promoter[33] to specifically label dI1 commissural axons in the chicken spinal cord. The chicken tubulin–GFP sequence was subcloned from a pCAG tubulin–GFP plasmid into one with the Math1 enhancer and the β-globin promoter. pCAG tubulin–GFP was a gift from Felicitas Proels and Martin Scaal (Addgene plasmid, 66105; http://n2t.net/addgene:66105; RRID: Addgene_66105)[70]. In ovo electroporation was performed as described previously in a video protocol[71]. In brief, plasmids were injected alone (td-Tomato-F plasmid) or together with the tubulin–GFP plasmid at a concentration of 700 ng μl^{-1} each in the central canal of the neural tube of stage HH17–18 chicken embryos[72]. A final concentration of 0.01% (v/v) of Fast Green was added to the plasmid mix to trace injection site and volume of the mix. Plasmids were unilaterally electroporated using a BTX ECM830 square-wave electroporator (five pulses at 25 V with 50-ms duration each). After electroporation, embryos were covered with sterile PBS, and eggs were sealed with tape and incubated at 39 °C for 26–30 h until embryos reached stage HH22.

Live imaging of intact chicken spinal cords

Dissection, mounting and imaging of intact spinal cords were performed as previously described[33]. Intact spinal cords were dissected from HH22 embryos and embedded, with the ventral side down, in a drop (100 µl) of 0.5% low-melting agarose (FMC) containing a 6:7 ratio of spinal cord medium (MEM with GlutaMAX (Gibco) supplemented with 4 mg ml^{-1} AlbuMAX (Gibco), 1 mM pyruvate (Sigma-Aldrich), 100 U ml^{-1} penicillin and 100 µg ml^{-1} streptomycin (both Gibco)) in a 35-mm ibidi µ-Dish with a glass bottom (ibidi, 81158). Once the agarose polymerized, 200 µl of spinal cord medium was added to the drop, and live imaging was started. Live imaging recordings were performed with an Olympus IX83 inverted microscope equipped with a spinning disk unit (CSU-X1, 10,000 r.p.m.; Yokogawa). Cultured spinal cords were kept at 37 °C with 5% CO_2 and 95% air in a PeCon cell vivo chamber. Temperature and CO_2 levels were controlled by the cell vivo temperature controller and the CO_2 controller units (PeCon). Spinal cords were incubated for at least 30 min before imaging was started. We acquired 35–40 planes (1.5-µm spacing) of 2 × 2 binned z-stack images every 5 min or 10 min for 12–24 h with a ×40 silicon oil objective (UPLSAPO S40x/1.25; Olympus) and an Orca-Flash 4.0 camera (Hamamatsu) with Olympus CellSens Dimension 2.2 software. Maximum projections of z-stack videos were generated and modified using Fiji/ImageJ[73]. Heat maps of tubulin–GFP intensities were generated with the 'Royal' lookup table, and growth cone boundaries were traced using the wand tool in Fiji/ImageJ. Kymographs were made with the KymoResliceWide plugin in Fiji/ImageJ.

Mathematical methods

We aimed to mathematically describe the stochastic processes underlying the selection of the future M-DCN axons while they project into the chiasma. Our approach consisted of three phases: (i) the analysis of the dynamics of axonal filopodia that project into the chiasma from ex vivo live imaging data; (ii) the formulation and parametrization of parsimonious models to describe the experimental data; and (iii) the simulation of the biological processes using these models to reproduce the data and make biologically testable predictions.

1. Initial filopodium growth dynamics

Filopodium extension and retraction. As shown in Fig. 4a,b, the number of filopodia per axons can be described by a Poisson distribution (with mean $\lambda_1 = 0.84$) at the initial timepoints of axon projection

into the chiasma (30 h APF and 31 h APF). We, thus, assumed that the initial filopodium dynamics can be described by a simple (linear) birth–death model[24]:

$$R_1 : A_{(f)} \rightarrow A_{(f+1)}, r_1 = \kappa \tag{S1.1}$$

$$R_2 : A_{(f)} \rightarrow A_{(f+1)}, r_2 = \delta \cdot f \tag{S1.2}$$

where the reactions R_1 and R_2 describe the processes of emergence of a new filopodium and the retraction of an existing filopodium within an axonal structure A. These reactions occur with reaction rates r_1 and r_2. The parameters κ and δ are the corresponding reaction parameters, and $A_{(f)}$ denotes an axonal structure with f number of filopodia. At the steady state, assuming the distribution of the number of filopodia follows a Poisson distribution $P(\lambda)$, we have that:

$$\lambda = \frac{\kappa}{\delta} = E[f] \tag{S1.3}$$

Parameter estimation. Next, we aimed to estimate the parameters of the model κ and δ. To that end, we defined the number of filopodium events as the number of changes (through emergence or retraction) in the number of filopodia in an axon between two consecutive timepoints. The probability to have a certain number of filopodium events $\#events = x$ can be written as:

$$P(x) = \sum_f P\left(A_{(f)}\right) \cdot P(x|f), \tag{S1.4}$$

where $P(A_{(f)})$ is the probability that an axon has f filopodia, and $P(x|f)$ is the conditional probability of the number of x filopodium events in an axon with f filopodia. At timepoints 30 h APF and 31 h APF, the probability of the number of filopodia $P(A_{(f)})$ follows a Poisson distribution with mean λ_1, $P(A_{(f)}) \sim \text{Poisson}(\lambda_1)$. Assuming that the probability distribution for the 'number of filopodium events' given the number of filopodia in an axon also follows a Poisson distribution, we have

$$P(x|f) \sim \text{Poisson}(\lambda_2), \text{with} \lambda_2 = (k + f \cdot \delta) \cdot \Delta t. \tag{S1.5}$$

Using S1.3, we can rewrite the previous expression for λ_2 as:

$$\lambda_2 = \left(k + f \cdot \frac{\kappa}{\lambda_1}\right) \cdot \Delta t. \tag{S1.6}$$

The probability density for $P(x|f)$ then reads:

$$P(x|f) = \frac{\left[\left(k + f \cdot \frac{\kappa}{\lambda_1}\right) \cdot \Delta t\right]^x \cdot e^{-\left(k + f \cdot \frac{\kappa}{\lambda_1}\right) \cdot \Delta t}}{x!}. \tag{S1.7}$$

The probabilities $P_{\text{data}}(x)$ and $P_{\text{data}}(A_{(f)})$ were taken directly from the data by plotting the histograms of the number of filopodium events x and the number of filopodia per axons, as shown in Supplementary Fig. 4a and Supplementary Fig. 4b, respectively. We can, thus, obtain estimates for κ and δ by:

$$\kappa^*, \delta^* = \underset{\kappa,\delta}{\text{argmin}}\, D_{KL}\left(P_{\text{data}}(x), \sum_f P_{\text{data}}\left(A_{(f)}\right) \cdot P(x|f)\right), \tag{S1.8}$$

where D_{KL} refers to the Kullback–Leibler divergence[74].

2. Filopodium stabilization dynamics

From 32 h APF, the measured distribution gradually deviates from the theoretical Poisson distribution (Fig. 4b). Although the initial filopodium dynamics can be described by a simple (linear) birth–death model reflecting filopodium extensions and retractions, other parameters might affect the filopodium dynamics at later timepoints. We, thus, assessed the survival probability of an axon related to its corresponding maximum number of filopodia throughout the observation time.

Data. The frequency of axon survival related to its corresponding maximum number of filopodia over time $N^{\max}_{\text{filopodia}}$ was calculated as:

$$\pi_{\text{SurvivalAxon}|N^{\max}_{\text{filopodia}}} = \frac{n_{\text{SelectedAxon}|N^{\max}_{\text{filopodia}}}}{n_{\text{TotalAxon}|N^{\max}_{\text{filopodia}}}} \tag{S1.9}$$

where $n_{\text{SelectedAxon}|N^{\max}_{\text{filopodia}}}$ denotes the number of selected axons (axons that target the medulla) given a certain $N^{\max}_{\text{filopodia}}$. Correspondingly, $n_{\text{TotalAxon}|N^{\max}_{\text{filopodia}}}$ denotes the total number of all axons projecting into the chiasma given a certain value of $N^{\max}_{\text{filopodia}}$. To account for the statistical uncertainty of the estimated survival frequencies of axons, the interquartile ranges were calculated using the Clopper–Pearson method[75].

Testing for independence. The frequencies for axon survival based on the data show a sharp increase in the survival probability for axons that contained a minimum of five filopodia (Fig. 4c). We compared the data-derived axon survival to a simple model assuming independence between the filopodia of an axon. Each filopodium has a fixed probability $P_{\text{Survival Filopodium}}$ to stabilize. We can write the probability for axon survival in the case where at least one filopodium of the structure survives as:

$$P_{\text{Survival Axon}|N^{\max}_{\text{filopodia}}} = 1 - (1 - P_{\text{Survival Filopodium}})^{N^{\max}_{\text{filopodia}}} \tag{S1.10}$$

with $N^{\max}_{\text{filopodia}}$ again denoting the maximum number of filopodia in an axon over time. From this equation, the more filopodia that are present in an axon, the more likely one of the filopodia will stabilize, and, thus, the axon survives to become a medulla targeting axon. If filopodia were independent from each other, the data-derived axon survival probabilities should follow equation (S1.10). Note that $P_{\text{Survival Filopodium}}$ is a free parameter. We tested a range of $P_{\text{Survival Filopodium}}$ and applied the one-sample Kolmogorov–Smirnov test to compare the data to the theoretical expectation.

3. Modeling filopodium dynamics

We extended the idea of a simple birth–death model to include a possible filopodium stabilization process that could describe the experimental data. This modeling approach describes the process of the filopodium extension, retraction and stabilization within an axon that projects in the chiasma. This model is described by the following reactions Rk and corresponding reaction rates rk, with $k = 1, 2, 3$:

$$R_1 : A_{(t,s)} \rightarrow A_{(t+1,s)}, r_1 = \kappa, \tag{S1.11}$$

$$R_2 : A_{(t,s)} \rightarrow A_{(t-1,s)}, r_2 = \delta \cdot t, \tag{S1.12}$$

$$R_3 : A_{(t,s)} \rightarrow A_{(t-1,s+1)}, r_3 = f(t) \cdot \gamma \cdot g_{\text{inhibition}}(s, B_{50}), \tag{S1.13}$$

where $A_{(t,s)}$ represents an axon with t transient and s stabilized filopodia. κ and δ are the previously data-derived parameters for filopodium emergence and retraction, respectively. γ is the stabilization rate parameter, and $g_{\text{inhibition}}(s, B_{50})$ is an auto-inhibition function dependent on the number of stabilized filopodia s and on the parameter B_{50}. This inhibition function is given by $g_{\text{inhibition}} = \frac{B_{50}}{s + B_{50}}$. $f(t)$ is given by $f(t) = \frac{t}{1 + e^{-(t-4)})}$, but it can also be replaced by $f(t) = t$ to derive the same conclusions.

Simulations of the M-DCN outcome. To test whether our model could predict our biological conditions, we performed 50,000 stochastic simulations for a developmental time of 20 h. This reflects the time window that covers the entire selection process from the beginning of the axon projection in the chiasma at 30 h APF to the observation of

the final adult pattern at 50 h APF from intravital live imaging (Fig. 2a). In the simulations, we calculated the proportion of medulla targeting axons among all simulated axons. To compare to the experimental numbers, we multiplied these simulated proportions by the experimental total number of axon projections into the chiasma ($n = 154$ on average).

Benchmarking the frame rate. To benchmark the frame rate (Supplementary Fig. 9e,f), we used a subset of the acquired data between 30 h APF and 32 h APF (frame rate $r_0 = 20$ min). We downsampled the data to simulate lower frame rates and measured the number of detected multi-filopodium axonal structures for each of the lower frame rates. These numbers were then compared to the number of detected multi-filopodium axonal structures at the baseline frame rate, r_0, of 20 min, resulting in a proportion of detected multi-filopodium axonal structures as a function of frame rate. Note that, during the downsampling procedure, a possible (temporal) offset of the initial observation time must be taken into account. This offset is an integer multiple of 20 min and is always lower than the considered frame rate. For example, let us assume a frame rate of 40 min; in this case, there are two possible offsets for observing the data: (i) observing the data at timepoints 0, 40, 80 and 120 min or (ii) observing the data at timepoints 20, 60, 100 and 140 min. The number of possible offsets was then used to calculate the detection probability of multi-filopodium axonal structures for a given frame rate r:

$$P_{\text{detected}}(r) = \frac{1}{N_{\text{offsets}}(r)} \sum_{j=1}^{N_{\text{offsets}}(r)} \frac{N_{\text{multi}}(r,j)}{N_{\text{multi}}(r_0,0)}, \tag{S1.14}$$

where N_{offsets} denotes the total number of possible offsets for the frame rate r. $N_{\text{multi}(r,j)}$ denotes the number of detected multi-filopodium axonal structures for frame rate r and offset j.

The measured probability of detected multi-filopodium axonal structures was then fitted with an inverse logistic function:

$$P_{\text{detected}}^{\text{theoretical}}(r) = \left(\frac{L}{1 + \exp\left(-k\left(r - a\right)\right)} + b \right)^{-1} \tag{S1.15}$$

with the four free parameters α, L, k and b.

Statistics and reproducibility

Sample sizes were not predefined based on statistical methods but were chosen based on the standard established in the field as reported in previous publications[3,11,13,43]. To account for the low number of individuals in live imaging, findings were supported and validated by fixed experiments with higher sample sizes. To avoid variability due to sex dimorphism, only *Drosophila* female individuals were dissected and analyzed. Female individuals were, however, randomly selected from fly vials at required developmental stage and adult age. When experiments involved multiple conditions, quantifications were done without knowing the genotype. Damaged brains were not imaged/quantified. Brains that did not develop during the live imaging session were excluded from analysis. No further data were excluded after quantification.

Statistical analyses were performed in R. In all our experiments, data distributions significantly deviated from a normal distribution with $P < 0.05$, using a Shapiro–Wilk test. We, therefore, systematically performed non-parametric tests: a two-sided Mann–Whitney *U*-test or a rank-based non-parametric Kruskal–Wallis test followed by a Dunn test when comparing more than two conditions. A Kolmogorov–Smirnov test was additionally performed to compare distributions (Supplementary Fig. 1h–j).

Detailed statistics

- Datasets related to Figs. 1h and 2b–d and Supplementary Fig. 1d–f(i). Sample brain 1 intravital imaging (29–50.5 h APF): $n = 1$, n(optic lobe) = 1, n(tracked projecting events) = 158. Sample brain 2 intravital imaging (32.5–44.3 h APF): $n = 1$, n(optic lobe) = 1, n(tracked projecting events) = 157.
- Datasets related to Fig. 3a–i. L3 m7GFP ($n = 8$, n(optic lobes) = 15): s.d. = 2.9, min = 1.0, Q1 = 4.5, median = 7.0, mean = 6.2, Q3 = 7.5, max = 13.0; s.d.% = 4.6, min = 2.8, Q1 = 9.5, median = 11.1, mean = 11.7, Q3 = 14.7, max = 21.0; (5 h APF m7GFP): $N = 3$, n(optic lobes)= 6, (s.d. = 2.9, min = 2.0, Q1 = 4.25, median = 6.0, mean = 6.0, Q3 = 7.75, max = 10.0), (s.d.% = 4.1, min = 5.1, Q1 = 8.9, median = 12.0, mean = 11.3, Q3 = 14.6, max = 15.9); (20 h APF m7GFP): $N = 4$, n(optic lobes) = 8, (s.d. = 2.8, min = 0.0, Q1 = 2.75, median = 5.0, mean = 4.5, Q3 = 6.0, max = 9.0), (s.d.% = 5.63, min = 0, Q1 = 6.8, median = 12.7, Q3 = 13.7, max = 16.2); (25 h APF m7GFP): $N = 4$, n(optic lobes) = 8, (s.d. = 5.1, min = 1.0, Q1 = 2.75, median = 4.5, mean = 6.1, Q3 = 8.5, max = 16.0), (s.d.% = 7.3, min = 2.6, Q1 = 5.2, median = 7.9, mean = 10.4, Q3 = 14.0, max = 22.7); (30 h APF m7GFP): $N = 3$, n(optic lobes) = 5, (s.d. = 2.2, min = 1.0, Q1 = 4.0, median = 5.0, mean = 4.25, Q3 = 5.25, max = 6), (s.d.% = 3.9, min = 2.6, Q1 = 7.7, median = 9.5, mean = 8.2, Q3 = 10.1, max = 11.2); (40 h APF m7GFP): $N = 2$, n(optic lobes) = 4, (s.d. = 2.5, min = 1.0, Q1 = 2.5, median = 3.5, mean = 3.75, Q3 = 4.75, max = 7.0), (s.d.% = 5.5, min = 2.9, Q1 = 6.4, median = 8.5, mean = 9.1, Q3 = 11.2, max = 16.3); (45 h APF m7GFP): $N = 2$, n(optic lobes) = 4, (s.d. = 0.5, min = 0.0, Q1 = 0.0, median = 0.0, mean = 0.25, Q3 = 0.25, max = 1.0), (s.d.% = 1.6, min = 0.0, Q1 = 0.0, median = 0.0, mean=0.81, Q3 = 0.81, max = 3.2); (50 h APF m7GFP): $N = 11$, n(optic lobes)= 6, (s.d.= 0.90, min = 0.0, Q1 = 0.0, median = 0.0, mean = 0.27, Q3 = 0.0, max = 3.0), (s.d.% = 0.94, min = 0.0, Q1 = 0.0, median = 0.0, mean = 0.28, Q3 = 0.0, max = 3.12).
- Datasets related to Fig. 3l. Sample brain 1 intravital imaging (27–47 h APF): $N = 1$, n(optic lobe) = 1, n(projecting events) = 3,902.
- Datasets related to Fig. 3p. (0 h APF + 27 h): $N = 3$, n(optic lobes) = 6; (24 h APF + 27 h): $N = 4$, n(optic lobes) = 7. Statistics: (0 h APF + 27 h versus 24 h APF + 27 h), Mann–Whitney *U*-test. W = 0, $P = 0.004624$.
- Datasets related to Fig. 3s–v. Supplementary Fig. 3a. (Ctrl Adult): $N = 9$, n(optic lobes) = 18; (N^{RNAi} Adult): $N = 10$, n(optic lobes) = 19; (Ctrl 36 h APF): $N = 5$, n(optic lobes) = 9. n(filopodia) = 163, n(multi-filopodia) = 86; (N^{RNAi} 36 h APF): $N = 6$, n(optic lobes) = 12, n(filopodia) = 248, n(multi-filopodia) = 186. • (Fig. 3s) Statistics: (Ctrl Adult versus N^{RNAi} Adult), Mann–Whitney *U*-test. $W = 37.5$, $P = 4.851 \times 10^{-5}$.
(Fig. 3v.) Statistics: (Ctrl 36 h APF versus N^{RNAi} 36 h APF), Mann–Whitney *U*-test. W = 3.5, $P = 0.0003528$. • (Supplementary Fig. 3a) Statistics: (Ctrl 36 h APF versus N^{RNAi} 36 h APF), Mann–Whitney *U*-test. W = 7378.5, $P = 0.329$. • Two-sample Kolmogorov–Smirnov test. $D = 01644$, $P = 0.4678$.
- Datasets related to Fig. 5e,f,h (brain 1). Sample intravital imaging (30–40 h APF): $N = 1$, n(optic lobe) = 1, n(tracked extending events) = 148.
- Datasets related to Fig. 5f,h (brain 2). Sample intravital imaging (30–40 h APF): $N = 1$, n(optic lobe) = 1, n(tracked extending events) = 215.
- Datasets related to Fig. 5k. (36 h APF): $N = 3$, n(optic lobes) = 6; (Adult): $N = 5$, n(optic lobes) = 9. Statistics: 36 h APF versus adult: Mann–Whitney *U*-test: $W = 23$, $P = 0.6733$.
- Datasets related to Fig. 5p. (Ctrl): $N = 16$, n(optic lobes) = 32; (N^{intra}): $N = 16$, n(optic lobes) = 32; (UAS-aTub84.GFP): $N = 15$, n(optic lobes) = 30; (N^{intra}; UAS-aTub84.GFP): $N = 7$, n(optic lobes) = 14. Statistics: Kruskal–Wallis test: Dunn chi-squared = 87.521, degrees of freedom (df) = 3, $P = 2.2 \times 10^{-16}$. Dunn test (Benjamini–Hochberg): Ctrl versus N^{intra}: 2.7725×10^{-9}; Ctrl versus UAS-aTub84.GFP: 0.002526; Ctrl versus N^{intra}; UAS-aTub84.GFP: 0.001059; UAS-aTub84.GFP versus N^{intra}: 5.1338×10^{-18}; UAS-aTub84.GFP versus N^{intra}; N^{intra}: 0.06715; UAS-aTub84.GFP versus N^{intra}; UAS-aTub84.GFP: 6.3975×10^{-8}.

- Datasets related to Fig. 6d(i) (yellow) and Supplementary Fig. 6c,d. (UAS-CD4.td-TOM): $N = 10$, n(optic lobes) = 20; (UAS-aTub84.GFP; UAS-CD4.td-TOM): $N = 12$, n(optic lobes) = 24. (Fig. 6d) Statistics: (UAS-CD4.td-TOM versus UAS-aTub84.GFP; UAS-CD4.td-TOM), Mann–Whitney U-test. $W = 144.5$, $P = 0.02331$. (Supplementary Fig. 5c) Statistics: (UAS-CD4.td-TOM versus UAS-aTub84.GFP; UAS-CD4.td-TOM), Mann–Whitney U-test. $W = 202.5$, $P = 0.3675$. (Supplementary Fig. 5d) Statistics: (UAS-CD4.td-TOM versus UAS-aTub84.GFP; UAS-CD4.td-TOM), Mann–Whitney U-test. $W = 225.5$, $P = 0.7396$.
- Datasets related to Fig. 6d(i) (gray). ($Ctrl^{shRNA}$): $N = 10$, n(optic lobes) = 16; ($alphaTub84B^{RNAi}$): $N = 8$, n(optic lobes) = 14; ($alphaTub85E^{RNAi}$): $N = 11$, n(optic lobes) = 21; ($alphaTub84D^{RNAi}$): $N = 11$, n(optic lobes) = 19. Statistics. Kruskal–Wallis test. Dunn chi-squared = 27.6905, df = 3, $P = 4.218 \times 10^{-6}$ • Dunn test (Benjamini–Hochberg) ($Ctrl^{shRNA}$ versus $alphaTub84B^{RNAi}$): 0.0094; ($Ctrl^{shRNA}$ versus $alphaTub85E^{RNAi}$): 0.0008. ($Ctrl^{shRNA}$ versus $alphaTub84D^{RNAi}$): 0.000; ($alphaTub84B^{RNAi}$ versus $alphaTub85E^{RNAi}$): 0.2780; ($alphaTub84B^{RNAi}$ versus $alphaTub84D^{RNAi}$): 0.0153; ($alphaTub84D^{RNAi}$ versus $alphaTub85E^{RNAi}$): 0.0316.
- Datasets related to Fig. 6d(ii) (green). (UAS-aTub84.GFP; $Ctrl^{shRNA}$): $N = 7$, n(optic lobes) = 14; (UAS-aTub84.GFP; alpha-$Tub84B^{RNAi}$): $N = 5$, n(optic lobes) = 10. (UAS-aTub84.GFP; $alphaTub85E^{RNAi}$): $N = 4$, n(optic lobes) = 8. (UAS-aTub84.GFP; $alphaTub84D^{RNAi}$): $N = 4$, n(optic lobes) = 8. Statistics: Kruskal–Wallis test. Dunn chi-squared = 1.75, df = 3, $P = 0.6259$. • Dunn test (Benjamini–Hochberg) (UAS-aTub84.GFP; $Ctrl^{shRNA}$ versus UAS-aTub84.GFP; $alphaTub84B^{RNAi}$): 0.3588. (UAS-aTub84.GFP; $Ctrl^{shRNA}$ versus UAS-aTub84.GFP; $alphaTub85E^{RNAi}$): 0.4644. (UAS-aTub84.GFP; $Ctrl^{shRNA}$ versus UAS-aTub84.GFP; $alphaTub84D^{RNAi}$): 0.5425. (UAS-aTub84.GFP; $alphaTub84B^{RNAi}$ versus UAS-aTub84.GFP; $alphaTub85E^{RNAi}$): 0.4399. (UAS-aTub84.GFP; $alphaTub84B^{RNAi}$ versus UAS-aTub84.GFP; $alphaTub84D^{RNAi}$): 0.5680. (UAS-aTub84.GFP; $alphaTub84D^{RNAi}$ versus UAS-aTub84.GFP; $alphaTub85E^{RNAi}$): 0.4658.
- Datasets related to Fig. 6y–z. (36 h APF Ctrl): $N = 2$, n(optic lobes) = 4. (36hAPF $shot^{shRNA}$): $N = 3$, n(optic lobes) = 6. (36 h APF $shot.LC^{OE}$): $N = 5$, n(optic lobes) = 9. (Fig. 6y) Statistics: Kruskal–Wallis test. Dunn chi-squared = 9.1171, df = 2, $P = 0.01048$. • Dunn test (Benjamini–Hochberg) (36 h APF Ctrl versus 36 h APF $shot^{shRNA}$): 0.0490; (36 h APF Ctrl versus 36 h APF $shot.LC^{OE}$): 0.0038; (36 h APF $shot^{shRNA}$ versus 36 h APF $shot.LC^{OE}$): 0.1185. (Fig. 6z) Statistics: Kruskal–Wallis test. Dunn chi-squared = 8.7343, df = 2, $P = 0.01269$. • Dunn test (Benjamini–Hochberg) (36 h APF Ctrl versus 36 h APF $shot^{shRNA}$): 0.0338; (36 h APF Ctrl versus 36 h APF $shot.LC^{OE}$): 0.0047; (36hAPF $shot^{shRNA}$ versus 36hAPF $shot.LC^{OE}$): 0.1809.
- Datasets related to Fig. 6AA,AB. (Adult Ctrl): $N = 15$, n(optic lobes) = 30; (Adult $shot^{shRNA}$): $N = 16$, n(optic lobes) = 31; (Adult $shot.LC^{OE}$): $N = 8$, n(optic lobes) = 16. (Fig. 6AA) Statistics: Kruskal–Wallis test. Dunn chi-squared = 39.452, df = 2, $P = 2.71 \times 10^{-9}$. • Dunn test (Benjamini–Hochberg) (Adult Ctrl versus Adult $shot^{shRNA}$): 0.0000; (Adult Ctrl versus Adult $shot.LC^{OE}$): 0.0107; (Adult $shot^{shRNA}$ versus Adult $shot.LC^{OE}$): 0.0000. (Fig. 6AB) Statistics: Kruskal–Wallis test. Dunn chi-squared = 5.6277, df = 3, $P = 0.05997$. • Dunn test (Benjamini–Hochberg) (Adult Ctrl versus Adult $shot^{shRNA}$): 0.3068**;** (Adult Ctrl versus Adult $shot.LC^{OE}$): 0.0423**;** (Adult $shot^{shRNA}$ versus Adult $shot.LC^{OE}$): 0.0309.
- Datasets related to Fig. 7d–f. (DMSO 30–36): $N = 10$, n(optic lobes) = 17; (Ncdzl 30–36): $N = 9$, n(optic lobes) = 17; (Fig. 7d) Statistics: (DMSO 30–36 versus Ncdzl 30–36), Mann–Whitney U-test. $W = 216$, $P = 0.01403$. (Fig.7e) Statistics: (DMSO 30–36 versus Ncdzl 30–36), Mann–Whitney U-test. $W = 257$, $P = 0.000113$. (Fig. 7f) Statistics: (DMSO 30–36 versus Ncdzl 30–36), Mann–Whitney U-test. $W = 249$, $P = 0.0003074$.
- Datasets related to Fig. 7j,k. (DMSO 48–54): $N = 4$, n(optic lobes) = 8. (Ncdzl 48–54): $N = 4$, n(optic lobes) = 7. (Fig. 7d) Statistics: (DMSO 48–54 versus Ncdzl 48–54), Mann–Whitney U-test. $W = 26.5$, $P = 0.9039$. (Fig. 7e) Statistics: (DMSO 48–54 versus Ncdzl 48–54), Mann–Whitney U-test. $W = 35.5$, $P = 0.4158$
- Datasets related to Supplementary Fig. 1h. (UAS-CD4.tdGFP; UAS-CD4.tdGFP, atoGAL4): $N = 25$, n(optic lobes) = 47.
- Datasets related to Supplementary Fig. 2d. (0 h APF NICD): $N = 6$, n(optic lobes) = 11; (10 h APF NICD): $N = 5$, n(optic lobes) = 10; (20 h APF NICD): $N = 4$, n(optic lobes) = 8; (30 h APF NICD): $N = 5$, n(optic lobes) = 8; (48 h APF NICD): $N = 3$, n(optic lobes) = 5; (0 h APF Ctrl): $N = 5$, n(optic lobes) = 7. Statistics: Kruskal–Wallis test. Dunn chi-squared = 48.528, df = 7, $P = 2.807 \times 10^{-8}$. • Dunn test (Benjamini–Hochberg) P values: (0 h APF NICD versus 10 h APF NICD): 0.4215; (0 h APF NICD versus 20 h APF NICD): 0.0009; (0 h APF NICD versus 30 h APF NICD): 0.0000; (0 h APF NICD versus 48 h APF NICD): 0.0005; (0 h APF NICD versus 0 h APF Ctrl): 0.0114; (10 h APF NICD versus 20 h APF NICD): 0.0007; (10 h APF NICD versus 30 h APF NICD): 0.0000; (10 h APF NICD versus 48 h APF NICD): 0.0005; (10 h APF NICD versus 0 h APF Ctrl): 0.0081; (20 h APF NICD versus 30 h APF NICD): 0.2342; (20 hAPF NICD versus 48 h APF NICD): 0.2992; (20 h APF NICD versus 0 h APF Ctrl): 0.2790; (30 h APF NICD versus 48 h APF NICD): 0.4133; (30 h APF NICD versus 0 h APF Ctrl): 0.0665; (48 h APF NICD versus 48 h APF NICD): 0.1445.
- Datasets related to Supplementary Fig. 2l–q. (Ctrl 36 h APF): $N = 3$, n(optic lobes) = 6; (N^{intra} 36 h APF): $N = 7$, n(optic lobes) = 10. Statistics: total filopodia (Ctrl 36 h APF versus N^{intra} 36 h APF), Mann–Whitney U-test. $W = 60$, $P = 0.001204$. Amplified axon (Ctrl 36 h APF versus N^{intra} 36 h APF), Mann–Whitney U-test. $W = 60$, $P = 0.0009642$. Tub^{GFP+} filopodia (Ctrl 36 h APF versus N^{intra} 36 h APF), Mann–Whitney U-test. $W = 60$, $P = 0.0006247$. Filopodia in LP (Ctrl 36 hAPF versus N^{intra} 36 h APF), Mann–Whitney U-test. $W = 60$, $P = 0.0008211$.
- Datasets related to Supplementary Fig. 5c,d. (Adult UAS-aTub84B.GFP; UAS-CD4.tdTom, atoGAL4): $N = 5$, n(optic lobes) = 6, n(filopodia) = 120, n(multi-filopodia) = 104; (36 h APF UAS-aTub84B.GFP; UAS-CD4.tdTom, atoGAL4): $N = 3$, n(optic lobes) = 9, n(filopodia) = 118, n(multi-filopodia) = 70. (Supplementary Fig. 5c) Statistics: (Ctrl 36 h APF versus N^{RNAi} *36* h APF), Mann–Whitney U-test. $W = 11708$, $P < 2.2 \times 10^{-16}$. • Two-sample Kolmogorov–Smirnov test. $D = 0.58729$, $P < 2.2 \times 10^{-16}$. (Supplementary Fig. 5d) Statistics: (Ctrl 36 h APF versus N^{RNAi} 36 h APF), Mann–Whitney U-test. $W = 3764.5$, $P = 0.5385$. • Two-sample Kolmogorov–Smirnov test. $D = 0.13606$, $P = 0.2285$.

Reporting summary

Further information on research design is available in the Nature Portfolio Reporting Summary linked to this article.

Data availability

Reagents and resources are listed in the Methods section of this paper and in Supplementary Table 1. The data required to support the findings of this study are available in the paper and in Supplementary Table 2. The mathematical model can be found in the 'Mathematical methods' section of the Methods.

References

58. Han, C., Jan, L. Y. & Jan, Y. N. Enhancer-driven membrane markers for analysis of nonautonomous mechanisms reveal neuron–glia interactions in *Drosophila*. *Proc. Natl Acad. Sci. USA* **108**, 9673–9678 (2011).

59. Nern, A., Pfeiffer, B. D. & Rubin, G. M. Optimized tools for multicolor stochastic labeling reveal diverse stereotyped cell arrangements in the fly visual system. *Proc. Natl Acad. Sci. USA* **112**, E2967–E2976 (2015).
60. Struhl, G. & Greenwald, I. Presenilin is required for activity and nuclear access of Notch in *Drosophila*. *Nature* **398**, 522–525 (1999).
61. Weinberger, S. et al. Evolutionary changes in transcription factor coding sequence quantitatively alter sensory organ development and function. *eLife* **6**, e26402 (2017).
62. Ngo, K. T., Andrade, I. & Hartenstein, V. Spatio-temporal pattern of neuronal differentiation in the *Drosophila* visual system: a user's guide to the dynamic morphology of the developing optic lobe. *Dev. Biol.* **428**, 1–24 (2017).
63. White, K. & Kankel, D. R. Patterns of cell division and cell movement in the formation of the imaginal nervous system in *Drosophila melanogaster*. *Dev. Biol.* **65**, 296–321 (1978).
64. Jennings, B., Preiss, A., Delidakis, C. & Bray, S. The Notch signalling pathway is required for *Enhancer of split* bHLH protein expression during neurogenesis in the *Drosophila* embryo. *Development* **120**, 3537–3548 (1994).
65. Lecourtois, M. & Schweisguth, F. The neurogenic Suppressor of Hairless DNA-binding protein mediates the transcriptional activation of the *Enhancer of split* Complex genes triggered by Notch signaling. *Genes Dev.* **9**, 2598–2608 (1995).
66. Bailey, A. M. & Posakony, J. W. Suppressor of Hairless directly activates transcription of *Enhancer of split* Complex genes in response to Notch receptor activity. *Genes Dev.* **9**, 2609–2622 (1995).
67. De Celis, J. F. et al. Functional relationships between *Notch*, *Su(H)* and the bHLH genes of the *E(spl)* complex: the E(spl) genes mediate only a subset of *Notch* activities during imaginal development. *Development* **122**, 2719–2728 (1996).
68. Krejčí, A., Bernard, F., Housden, B. E., Collins, S. & Bray, S. J. Direct response to Notch activation: signaling crosstalk and incoherent logic. *Sci. Signal.* **2**, ra1 (2009).
69. Assa-Kunik, E., Torres, I. L., Schejter, E. D., St Johnston, D. & Shilo, B. Z. *Drosophila* follicle cells are patterned by multiple levels of Notch signaling and antagonism between the Notch and JAK/STAT pathways. *Development* **134**, 1161–1169 (2007).
70. Sagar, Pröls, F., Wiegreffe, C. & Scaal, M. Communication between distant epithelial cells by filopodia-like protrusions during embryonic development. *Development* **142**, 665–671 (2015).
71. Wilson, N. H. & Stoeckli, E. T. In ovo electroporation of miRNA-based plasmids in the developing neural tube and assessment of phenotypes by DiI injection in open-book preparations. *J. Vis. Exp.* **16**, 4384 (2012).
72. Hamburger, V. & Hamilton, H. L. A series of normal stages in the development of the chick embryo. *J. Morphol.* **88**, 49–92 (1951).
73. Schindelin, J. et al. Fiji: an open-source platform for biological-image analysis. *Nat. Methods* **9**, 676–682 (2012).
74. Kullback, S. & Leibler, R. A. On information and sufficiency. *Ann. Math. Stat.* **22**, 79–86 (1951).
75. Clopper, C. J. & Pearson, E. S. The use of confidence or fiducial limits illustrated in the case of the binomial. *Biometrika* **26**, 404–413 (1934).

Acknowledgements

The authors thank the Bloomington Stock Center (NIH P40OD018537), the Vienna Drosophila Resource Center, the Developmental Studies Hybridoma Bank, E. A. Kravitz and A. Hasan for flies and reagents; B. Kunz, T. Flego, L. Hellbruegge and R. Cook for technical assistance; and H. Wolfenberg, D. Johannes and N. Demirbas for animal care and help with fly stock management. We thank C. Desplan, N. Renier and all members of the Hassan, Hiesinger and Wernet laboratories for support, insightful discussion and valuable comments. Light microscopy was carried out in the laboratory of P.R.H. at Freie Universität Berlin and in the ICM.Quant core facility of the Paris Brain Institute (ICM). We gratefully acknowledge C. Lovo for her advice on the use of Bruker multiphoton. This work was supported by the Einstein-BIH program (to B.A.H. and P.R.H.), Deutsche Forschungsgemeinschaft (DFG) Research Unit 5289 RobustCircuit project P2 (to B.A.H. and P.R.H.) and RobustCircuit project Z1 (to M.v.K. and P.R.H.); DFG Research Unit Syntophagy RP7 (Hi 1886/8); funding from the European Research Council under the European Union's Horizon 2020 Research and Innovation Programme (101019191) (to P.R.H.); the Investissements d'Avenir program (ANR-10-IAIHU-06); Paris Brain Institute-ICM core funding; the Paul G. Allen Frontiers Group Allen Distinguished Investigator grant; the Roger De Spoelberch Prize; an NIH Brain Initiative R01 grant (1R01NS121874-01) (to B.A.H.); the Fondation de la Recherche Medical (FRM) postdoctoral fellowship (ARF202005011913 to M.A.); the Swiss National Science Foundation (310030_185247) (to E.S.); DFG grant number 450430223 (to C.B. and M.v.K.); and the DFG under Germany´s Excellence Strategy–Berlin Mathematics Research Center MATH+ (EXC-2046/1, project ID: 390685689) (to M.v.K.). The funders had no role in the design of the study or the decision to publish.

Author contributions

M.A., P.R.H. and B.A.H. conceived the project. M.A. designed, performed and analyzed all *Drosophila* experiments. T.T.G. helped with microscope scanning and quantifications. M.A. and S.B.D. established the ex vivo culture protocol for DCN live imaging. A.D. and E.S. conceived, designed, performed and analyzed all chicken experiments. C.B., E.R. and M.v.K. conceived, designed, performed and analyzed all the mathematical computational modeling work. M.A. and B.A.H. wrote the manuscript, and all authors provided critical feedback. M.A., M.v.K., E.S., P.R.H. and B.A.H. acquired funding.

Competing interests

The authors declare no competing interests.

Additional information

Supplementary information The online version contains supplementary material available at https://doi.org/10.1038/s41593-025-01937-y.

Correspondence and requests for materials should be addressed to Bassem A. Hassan.

Peer review information *Nature Neuroscience* thanks Chihiro Hama and the other, anonymous, reviewer(s) for their contribution to the peer review of this work.

nature portfolio

Corresponding author(s): Dr. Bassem Hassan

Last updated by author(s): 06/02/2025

Reporting Summary

Nature Portfolio wishes to improve the reproducibility of the work that we publish. This form provides structure for consistency and transparency in reporting. For further information on Nature Portfolio policies, see our Editorial Policies and the Editorial Policy Checklist.

Statistics

For all statistical analyses, confirm that the following items are present in the figure legend, table legend, main text, or Methods section.

n/a	Confirmed	
☐	☒	The exact sample size (*n*) for each experimental group/condition, given as a discrete number and unit of measurement
☐	☒	A statement on whether measurements were taken from distinct samples or whether the same sample was measured repeatedly
☐	☒	The statistical test(s) used AND whether they are one- or two-sided *Only common tests should be described solely by name; describe more complex techniques in the Methods section.*
☒	☐	A description of all covariates tested
☒	☐	A description of any assumptions or corrections, such as tests of normality and adjustment for multiple comparisons
☐	☒	A full description of the statistical parameters including central tendency (e.g. means) or other basic estimates (e.g. regression coefficient) AND variation (e.g. standard deviation) or associated estimates of uncertainty (e.g. confidence intervals)
☐	☒	For null hypothesis testing, the test statistic (e.g. *F*, *t*, *r*) with confidence intervals, effect sizes, degrees of freedom and *P* value noted *Give P values as exact values whenever suitable.*
☒	☐	For Bayesian analysis, information on the choice of priors and Markov chain Monte Carlo settings
☒	☐	For hierarchical and complex designs, identification of the appropriate level for tests and full reporting of outcomes
☒	☐	Estimates of effect sizes (e.g. Cohen's *d*, Pearson's *r*), indicating how they were calculated

Our web collection on statistics for biologists contains articles on many of the points above.

Software and code

Policy information about availability of computer code

Data collection

• Fixed Drosophila brain samples were imaged using a Leica TCS SP8-X white laser confocal microscope with a 63X glycerol objective (NA=1.3).
• Drosophila Live imaging experiments were acquired at 25°C, on a Leica SP8 MP 2-photon microscope with a 40X IRAPO water objective (NA=1.1), a Chameleon Ti:Sapphire laser and Resonant scanner with a single excitation laser at 896nm for either one color imaging (GFP) two color imaging (GFP/Tomato), Image resolution: 1024x1024, Resonance scanner, dwell time : 0.8. Intravital imaging parameters – laser power: 40%, Gain: 40%. Ex-vivo imaging parameters – Lazer power: 5%, Gain: 40%.
The Nocodazole and EB1-GFP ex-vivo Live imaging experiments were acquired on a Ultima 2Pplus Bruker 2-photon microscope with a N20X-PFH - 20X Olympus XLUMPLFLN Objective (1.00 NA, 2.0 mm WD), 920nm excitation laser, Image resolution: 1024x1024, Galvo scanner, Lazer power: 120%, dwell time : 0.8.

• Live imaging of intact chicken spinal cords were performed with an Olympus IX83 inverted microscope equipped with a spinning disk unit (CSU-X1 10'000 rpm, Yokogawa), with a 40x silicon oil objective (UPLSAPO S40x/1.25, Olympus) and an Orca-Flash 4.0 camera (Hamamatsu) with the help of Olympus CellSens Dimension 2.2 software.

Data analysis	• Imaris software 10.1.0 (2023 Nov 15) (Bitplane, Switzerland) with the following modules was used to visualize and analyze the Drosophila data (See methods section): 'Image Alignement'; 'oblique-slice'; 'mask module'; 'Filament Tracer'; 'TrackingLineage'. • Maximum projections of Z-stack Chick embryo videos were generated and modified using Fiji/ImageJ2 version 2.14.0/1.54f. Heat maps of tubulin-GFP intensities were generated with the "Royal" Lookup table and growth cone boundaries were traced using the wand tool in Fiji/ImageJ. • Statistical analyses were performed in R version 4.2.1 (2022-06-23). • Figures were assembled with Adobe Photoshop 2022 (23.0.0 Release).

For manuscripts utilizing custom algorithms or software that are central to the research but not yet described in published literature, software must be made available to editors and reviewers. We strongly encourage code deposition in a community repository (e.g. GitHub). See the Nature Portfolio guidelines for submitting code & software for further information.

Data

Policy information about availability of data

All manuscripts must include a data availability statement. This statement should provide the following information, where applicable:

- Accession codes, unique identifiers, or web links for publicly available datasets
- A description of any restrictions on data availability
- For clinical datasets or third party data, please ensure that the statement adheres to our policy

The Data required to support the finding of this paper are available in the manuscript and supplementary files. The Mathematical model can be found in the Supplementary Information "Supplementary Mathematical Methods".

Research involving human participants, their data, or biological material

Policy information about studies with human participants or human data. See also policy information about sex, gender (identity/presentation), and sexual orientation and race, ethnicity and racism.

Reporting on sex and gender	N/A
Reporting on race, ethnicity, or other socially relevant groupings	N/A
Population characteristics	N/A
Recruitment	N/A
Ethics oversight	N/A

Note that full information on the approval of the study protocol must also be provided in the manuscript.

Field-specific reporting

Please select the one below that is the best fit for your research. If you are not sure, read the appropriate sections before making your selection.

☒ Life sciences ☐ Behavioural & social sciences ☐ Ecological, evolutionary & environmental sciences

For a reference copy of the document with all sections, see nature.com/documents/nr-reporting-summary-flat.pdf

Life sciences study design

All studies must disclose on these points even when the disclosure is negative.

Sample size	Sample sizes were not predefined based on statistical methods but were chosen based on the standard established in the field as reported in previous publications (see references 3,11,13,43). To account for the low number of individuals in Live imaging, findings were supported and validated by fixed experiments with higher sample sizes.
Data exclusions	- To avoid variability due to sex dimorphism, only Drosophila female individuals were dissected and analyzed. Damaged brains were not imaged/quantified. As well brains that did not develop during the live imaging session. No data was excluded post-quantification. - Out of focus imaged brains and non-developed brains during live imaging experiments were excluded from analysis.
Replication	Experiments were repeated at least two times from independent crosses. All replications attempts were successful.
Randomization	Female individuals were randomly selected from fly vials at required developmental stage and adult age.
Blinding	When experiments involved multiple conditions (at least two), quantifications were done without knowing the genotype.

Reporting for specific materials, systems and methods

We require information from authors about some types of materials, experimental systems and methods used in many studies. Here, indicate whether each material, system or method listed is relevant to your study. If you are not sure if a list item applies to your research, read the appropriate section before selecting a response.

Materials & experimental systems

n/a	Involved in the study
☐	☒ Antibodies
☒	☐ Eukaryotic cell lines
☒	☐ Palaeontology and archaeology
☐	☒ Animals and other organisms
☒	☐ Clinical data
☒	☐ Dual use research of concern
☒	☐ Plants

Methods

n/a	Involved in the study
☒	☐ ChIP-seq
☒	☐ Flow cytometry
☒	☐ MRI-based neuroimaging

Antibodies

Antibodies used

- Chicken anti-GFP [1:500, Abcam Cat# AB13970; RRID: AB_300798]
- Goat anti-GFP [1:500, Abcam Cat# ab6678, RRID:AB_2042708]
- Rabbit anti-mCherry [1:500, Abcam Cat# ab167453, RRID:AB_2571870]
- Rabbit anti-dsRed [1:200, Takara Bio Cat# 632496, RRID: AB_10013483]
- Rat cadherin, DN- (extracellular domain) antibody [1:50, Developmental Studies Hybridoma Bank Cat# DN-Ex #8, RRID: AB_528121]
- Rat monoclonal anti-Flag DYKDDDDK [1:200, Novusbio Cat# NBP1-067-12 clone L5, RRID:AB_1625982]
- Rabbit HA-Tag (C29F4) Rabbit mAb antibody [1:300, Cell Signalling Cat# 3724, RRID:AB_1549585]
- Mouse Anti-Viral V5-TAG Monoclonal antibody, Unconjugated, Clone SV5-Pk1 [1:500, BioRad Cat# MCA1360, RRID:AB_322378]
- Alexa Fluor® 488 AffiniPure Donkey Anti-Chicken IgY (IgG) (H+L) [1:500, Jackson ImmunoResearch Labs Cat# 703-545-155, AB_2340375]
- Alexa Fluor® 647 AffiniPure Donkey Anti-Rat IgG (H+L) [1:500, Jackson ImmunoResearch Labs Cat#712-605-153, RRID: AB_2340694]
- Cy™3 AffiniPure Donkey Anti-Mouse IgG (H+L) [:500, Jackson ImmunoResearch Labs Cat#715-165-151, RRID: AB_2315777]
- DyLight™ 405 AffiniPure Donkey Anti-Rabbit IgG (H+L) [1:500, Jackson ImmunoResearch Labs, Cat#711-475-152, RRID: AB_2340616]
- Cy™3 AffiniPure Donkey Anti-Rabbit IgG (H+L) [1:500, Jackson ImmunoResearch Labs, Cat#711-165-152, RRID: AB_2307443]
- Alexa Fluor® 488 AffiniPure Donkey Anti-Goat IgG (H+L) [1:500, Jackson ImmunoResearch Labs, Cat#705-545-003, RRID: AB_2340428]

Validation

All used antibodies have been published previously, and are used to enhance of detect genomicaly tagged proteins.

Animals and other research organisms

Policy information about studies involving animals; ARRIVE guidelines recommended for reporting animal research, and Sex and Gender in Research

Laboratory animals

For all experiments, flies were crossed and aged at 25°C when not specified. Temporal Optogenetic activation of Notch – Fly crosses were kept in dark at 25°C. Females F1 white pupae (0hAPF) were collected under red light and raised in dark at 25°C until the indicated time point of blue light exposure.

The following fly stocks were used: ato.14A-GAL4 (BDSC#6480)1, UAS-CD4-tdGFP on 2nd and 3rd chromosomes (BDSC#35839 and BDSC#35836)2, UAS-CD4-tdTomato (III) (BDSC#35837)2, pBPhsFlp2::PEST (X)3, UAS-FRT-STOP-FRT.CD4-tdGFP, hey-GFP.FPTB (III) (BDSC#64826), [Hey:T2A:FLP, UAS-myr :GFP, UAS-FRT-STOP-FRT-myr:sfGdP:HA] (Gift from Doe lab)4, [e(spl)-C-GFPm7]BAC (Gift from Schweisguth lab)5, UAS-NotchdsRNA (BDSC#7077), UAS-Notchintra.GS (BDSC#52008) 6, lexAop-Notchintra 7, UAS-CIBN::LexA-mcherry-p65::CRY2 (Gift from Kravitz lab)8, UAS-LifeAct.RFP (III) (BDSC#58362), UAS-Lifeact-Ruby (II) (BDSC#35545), UASp-GFPS65C-alphaTub84B on 2nd and 3rd chromosomes (BDSC#7374 and BDSC#7373) 9, UAS-EGFP (X) (BDSC#5428), pBPhsFlp2::PEST;;10UAS-HA_V5_FLAG 3, UAS-EB1-GFP (III) (BDSC#35512), shRNA control (VDRC#60200), UAS-tub84B RNAi (VDRC#33427), UAS-tub84D RNAi (VDRC#330509), UAS-tub85E RNAi (VDRC#330369), UAS-shot.L(C)GFP (BDSC#29042), UAS-shot.L(A)GFP (BDSC#29044), UAS-shot shRNA (VDRC#330586).
Flies were dissected at 1 week-old adult stage, or developmental stages (L3, 5hAPF, 20hAPF, 25hAPF, 30hAPF, 36hAPF, 40hAPF, 44hAPF, 45hAPF, 50hAPF).
The detailed fly genotypes for all figures can be found in the supplementary material.

The following Chicken strain was used and embryos were reared at 39°C: Hubbard JA57 strain Hubbard LLC Cat#: Brüterei Stöckli, Ohmstal.

Wild animals

This study does not use wild animals.

Reporting on sex

For pupal staged developmental experiment, female Drosophila melanogaster were selected at 0hAPF (white pupae) based on the

Reporting on sex	absence of male gonads. For adult sample collection, female adult flies were selected based on the absence of sex comb. No sex selection was done for chicken experiments.
Field-collected samples	This study does not use field-collected samples.
Ethics oversight	This study does not require ethical approvals.

Note that full information on the approval of the study protocol must also be provided in the manuscript.